*Nature Communications* **13**, 2140 (2022), https://doi.org/10.1038/s41467-022-29791-7;
preprint dated 2021-09-13: https://doi.org/10.33774/chemrxiv-2021-tt6sx

# Low Energy Carbon Capture via Electrochemically Induced pH Swing with Electrochemical Rebalancing

Shijian Jin[†], Min Wu[†], Yan Jing[‡], Roy G. Gordon[‡] and Michael J. Aziz[†*]

[†] John A. Paulson School of Engineering and Applied Sciences, Harvard University, Cambridge, Massachusetts, 02138, United States

[‡]Department of Chemistry and Chemical Biology, Harvard University, Cambridge, Massachusetts 02138, United States

*maziz [at] harvard [dot] edu

## Abstract

We demonstrate a carbon capture system based on pH swing cycles driven through proton-coupled electron transfer of sodium (3,3'-(phenazine-2,3-diylbis(oxy))bis(propane-1-sulfonate)) (DSPZ) molecules. Electrochemical reduction of DSPZ causes an increase of hydroxide concentration, which absorbs $CO_2$; subsequent electrochemical oxidation of the reduced DSPZ consumes the hydroxide, causing $CO_2$ outgassing. The measured electrical work of separating $CO_2$ from a binary mixture with $N_2$, at $CO_2$ inlet partial pressures ranging from 0.1 to 0.5 bar, and releasing to a pure $CO_2$ exit stream at 1.0 bar, was measured for electrical current densities of 20 to 150 mA $cm^{-2}$. The work for separating $CO_2$ from a 0.1 bar inlet and concentrating into a 1 bar exit is 61.3 kJ $mol_{CO2}^{-1}$ at a current density of 20 mA $cm^{-2}$. Depending on the initial composition of the electrolyte, the molar cycle work for capture from 0.4 mbar extrapolates to 121-237 kJ $mol_{CO2}^{-1}$ at 20 mA $cm^{-2}$. We also introduce an electrochemical rebalancing method that extends cell lifetime by recovering the initial electrolyte composition after it is perturbed by side reactions. We discuss the implications of these results for future low-energy electrochemical carbon capture devices.

## Introduction

Accumulating $CO_2$ emissions from anthropogenic activities constitute the major cause of global climate change.[1,2] While efforts are being made in switching from fossil fuel-based energy to virtually emissions-free sources such as nuclear, solar, wind and geothermal, fossil fuel combustion will remain an important component of the world economy for a long time.[3] Consequently, carbon removal — whether captured from a point source[2,4-8] such as a combustion power plant or directly from the air (a.k.a. direct air capture, DAC) or the ocean[2,9-13] — in order to reduce atmospheric $CO_2$ concentrations, is gaining increasing attention.

Numerous methods for point source capture and DAC have been developed. Among the most studied is wet amine scrubbing for point source capture[4-6] and strongly alkaline (pH > 14) solution for DAC,[2,9] both of which rely on a large temperature-swing cycle to regenerate sorbents. Although sorbent composition has been optimized to lower the energy cost for both strategies, the thermal energy requirement for heating is still ~100 kJ $mol_{CO2}^{-1}$ for point source

capture[6,14,15] and >150 kJ $mol_{CO2}^{-1}$ for DAC.[10,16] In addition, sorbent volatility, toxicity and corrosivity cause environmental concerns.[2] Methods that remove $CO_2$ from the ocean, which allow it to absorb more $CO_2$, have also been studied, but the high water-handling requirement is a challenge.[12,13]

Electrochemically mediated separation technologies constitute an increasingly attractive alternative to traditional temperature-swing or pressure-swing methods because of the rapidly decreasing cost of intermittent renewable electricity and the mild operating conditions of ambient temperature and pressure.[7,8,13,17-20] However, most existing methods operate at low current density (< 5 mA $cm^{-2}$) because of large overpotentials and the corresponding energetic cost at higher current density, implying a high capital cost of electrochemical hardware. Recently, our group proposed and demonstrated a pH swing cycle for $CO_2$ separation electrochemically driven through proton-coupled electron transfer (PCET) of redox active organic molecules ("Q").[18] In this scheme, proton-coupled electrochemical reduction of these molecules ($Q + 2H_2O + 2e^- \rightarrow QH_2 + 2OH^-$) raises the electrolyte pH and total alkalinity (TA), leading to $CO_2$ capture from point source or air and conversion to dissolved inorganic carbon (DIC); subsequent electrochemical oxidation of the reduced molecules ($QH_2 + 2OH^- \rightarrow Q + 2H_2O + 2e^-$) acidifies the electrolyte and lowers TA, resulting in the conversion of DIC to $CO_2$ gas and its release.

Here, we report a proof-of-concept point source (10 %) $CO_2$ separation system that uses a sodium (3,3'-(phenazine-2,3-diylbis(oxy))bis(propane-1-sulfonate)), i.e. DSPZ (**Fig. 1a**), based electrochemical pH-swing cell with an energy cost of only 61.3 kJ $mol_{CO2}^{-1}$ at 20 mA $cm^{-2}$. Through analyzing the cycle work obtained under systematically varied inlet partial pressure and current density, we estimate that the cost for capturing from a 0.4 mbar $CO_2$ inlet using this system extrapolates to 108–212 kJ $mol_{CO2}^{-1}$ in the low-current-density limit, and that it can be further lowered if a higher concentration of DSPZ, or other PCET-active molecules, is used. Recognizing the sensitivity of the reduced form of DSPZ, i.e. $DSPZH_2$, to chemical oxidation by atmospheric or dissolved $O_2$, we introduce and demonstrate an electrochemical rebalancing method that expels oxygen from solution and restores the initial composition of the electrolytes.

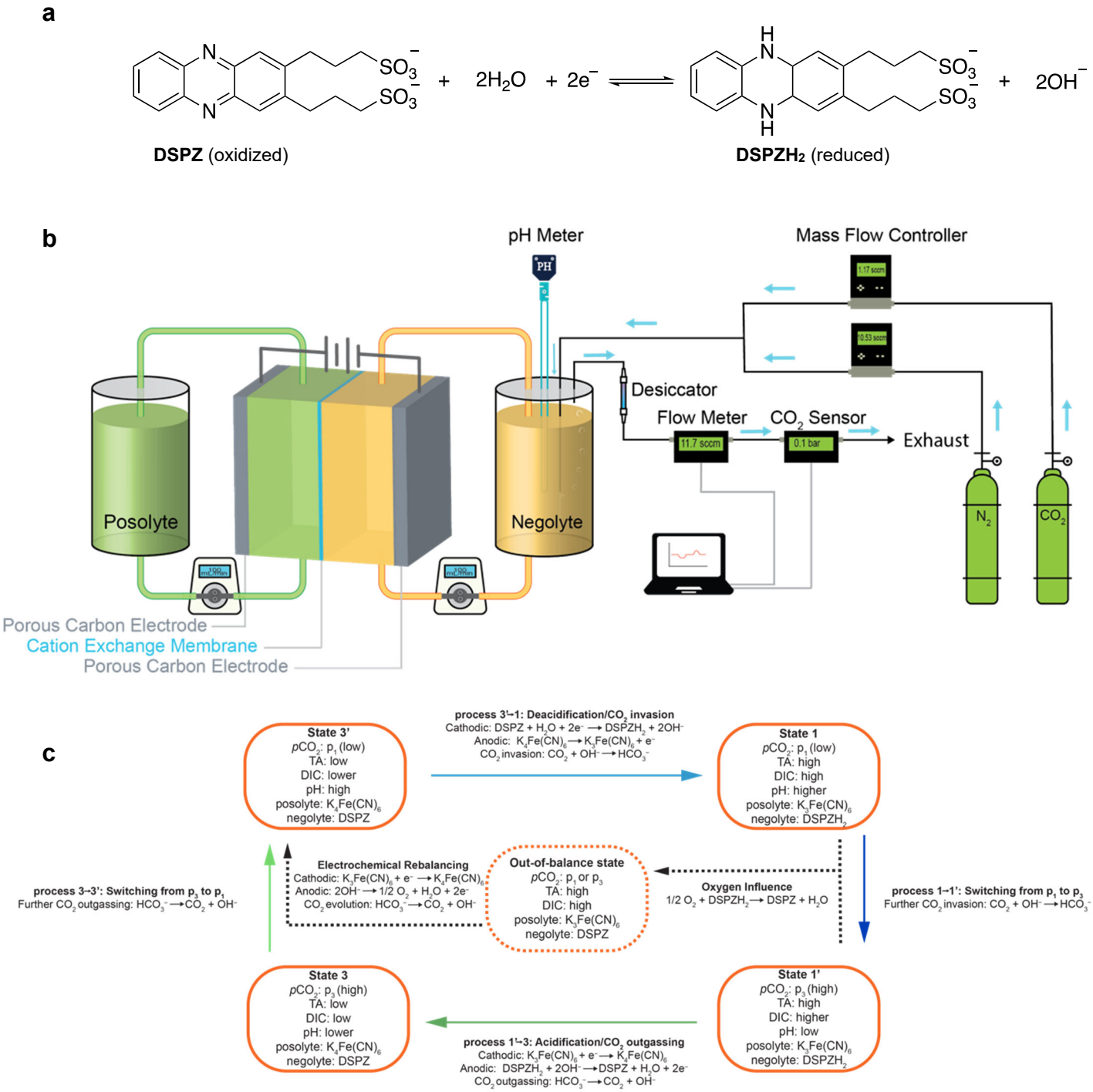


**Fig. 1| Scheme of the pH swing carbon capture flow system. a,** Schematic of the reversible PCET reaction underwent by DSPZ in an aqueous solution. **b**, Schematic of the $Fe(CN)_6$ (posolyte) | DSPZ (negolyte) flow cell and full system. Blue arrows indicate gas flow direction. Adapted from Jin *et al*.[18] **c**, Process flow. The solid arrows refer to desired reactions in a complete carbon capture/release cycle. The carbonate formation and decomposition reactions are neglected for simplicity. The dashed arrow on the right side refers to the side reaction caused by oxygen and the dashed arrow on the left refers to reactions in the electrochemical rebalancing step.

**Device Setup and Process Flow**

**Fig. 1b** shows the schematic of the $Fe(CN)_6$ | DSPZ carbon capture flow cell and the hardware for providing the gas mixture and analyzing the exhaust. The upstream gas composition in the negolyte headspace was controlled by $CO_2$ and $N_2$ mass flow controllers (MFCs). Downstream of the negolyte reservoir, the gas was dried with a desiccator and the total gas flow rate and $CO_2$ partial pressure were measured using a digital flow meter and a $CO_2$ sensor, respectively. A pH probe immersed in the negolyte solution reported the temporal evolution of its pH, which enabled the tracking of total alkalinity (TA) and dissolved inorganic carbon (DIC) in real time. **Fig. 1c** illustrates the electrolyte composition in the four states of the pH swing carbon capture cycle and the processes connecting the states. We denote the $CO_2$ partial pressure during the $CO_2$ capture process as the inlet pressure or $p_1$, and that during the $CO_2$ outgassing process as the exit pressure or $p_3$, which is always set to 1 bar (100% $CO_2$) in this study. Similarly, the subscripts following TA or DIC refer to the TA and DIC of the corresponding states. The naming convention for the states is adopted from previous work,[18] where the equilibrium and constraints governing pH, TA, DIC and $pCO_2$ are explained in detail.

The four colored arrows in **Fig. 1c** refer to the four processes in the carbon capture cycle. The four sequential processes are as follows: $3'_i \rightarrow 1$: two-stage deacidification+$CO_2$ invasion (inlet). In this process, DSPZ is electrochemically reduced to $DSPZH_2$ and hydroxide is produced, which reacts with $CO_2$ to form carbonate/bicarbonate. $1 \rightarrow 1'$: change of the headspace atmosphere from inlet to exit pressure, i.e. switching from $p_1$ to $p_3$. $1' \rightarrow 3$: two-stage acidification+$CO_2$ outgassing (exit). In this process $DSPZH_2$ is electrochemically oxidized to DSPZ and hydroxide is consumed, which in turn leads to carbonate/bicarbonate decomposition and $CO_2$ evolution. $3 \rightarrow 3'_f$: change of the headspace atmosphere from exit to inlet pressure, i.e. switching from $p_3$ to $p_1$. The change in TA and DIC in these processes are denoted with $\Delta TA_{a\rightarrow b}$ and $\Delta DIC_{a\rightarrow b}$, respectively, where the subscript refers to process "a→b", and a and b are any pairs of states. An example cycle is described quantitatively in the next section.

As $DSPZH_2$ is reversibly chemically oxidized by atmospheric $O_2$ to DSPZ (right dashed arrow in **Fig. 1c**), the posolyte supplies extra charge to electrochemically reduce the extra oxidized DSPZ; this is reflected in the low Coulombic efficiency of the cell and an accumulation of TA and DIC in the negolyte. This process also transforms more of the posolyte to its oxidized form, i.e. $[K^+]_4[Fe^{II}(CN)_6]^{4-} \rightarrow [K^+]_3[Fe^{III}(CN)_6]^{3-} + K^+ + e^-$, than at a similar point in the previous deacidification-acidification cycle. During cell operation reduction on one side must be accompanied by oxidation on the other side but, as the available fraction of reduced species on the posolyte side, i.e. $[K^+]_4[Fe^{II}(CN)_6]^{4-}$, decreases, the cell can access less and less of its theoretical capacity during its oxidation-reduction oscillations; this is reflected in the decaying capacity of the cell. Eventually both sides become 100% oxidized and cell operation ceases. Our remedy for such situations is the electrochemical rebalancing method (left dashed arrow in **Fig. 1c**) explained later in the text.

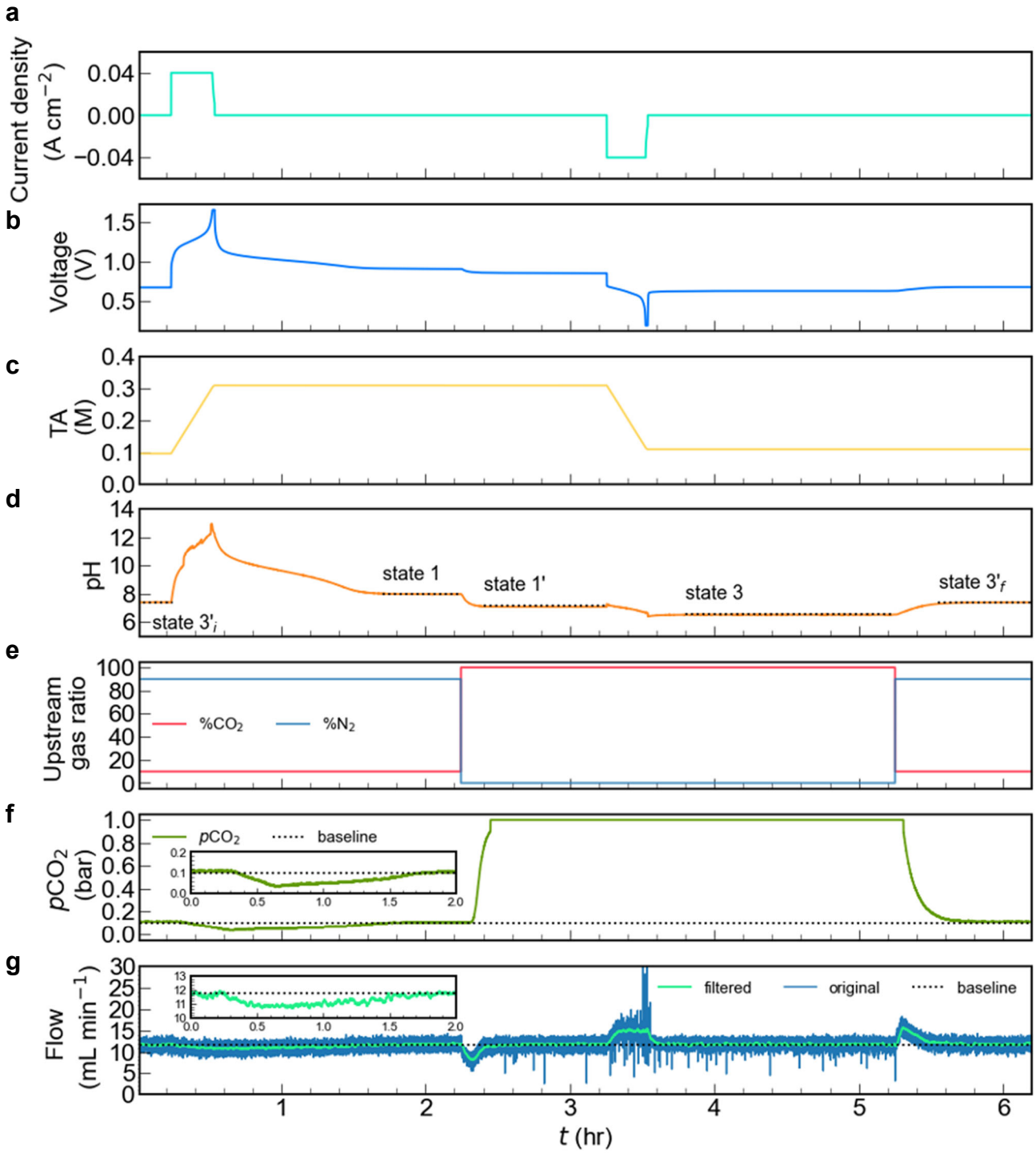


**Fig. 2| A $CO_2$ concentrating cycle with inlet pressure $p_1$ = 0.1 bar and exit pressure $p_3$ = 1 bar using a DSPZ-based flow cell at 40 mA cm$^{-2}$.** Electrolytes comprised 10 mL 0.11 M DSPZ in 1 M KCl (negolyte, capacity limiting) and 35 mL 0.1 M $K_4Fe(CN)_6$ and 0.04 M $K_3Fe(CN)_6$ in 1 M KCl (posolyte, non-capacity limiting). **a,** Current density. **b,** Voltage. **c,** Total alkalinity. **d,** pH of the negolyte. States 3'$_i$, 1, 1', 3 and 3'$_f$ represent pH values before deacidification under 0.1 bar $pCO_2$, after deacidification+absorption under 0.1 bar $pCO_2$, after changing $pCO_2$ from 0.1 bar to 1 bar, after acidification+desorption under 1 bar and after changing $pCO_2$ from 1 bar to 0.1 bar, respectively. The detailed composition of these states is elaborated in **Table 1**. **e** $N_2$ and $CO_2$ percentage in the upstream source gas, controlled by mass flow controllers. **f,** downstream $CO_2$ partial pressure. The baseline indicates $pCO_2$ = 0.1 bar. Inset: Zoomed-in view of downstream $CO_2$ partial pressure in between 0< $t$ < 2 hr, where $CO_2$ capture takes place. **g,** downstream

total gas flow rate; the baseline is 11.8 mL $min^{-1}$. Inset: Zoomed-in view of downstream gas flow rate (filtered) in between $0< t < 2$ hr, where $CO_2$ capture takes place.

## One Carbon Capture Cycle with $p_1$ = 0.1 bar and $p_3$ =1 bar at 40 mA $cm^{-2}$

In previous work we demonstrated a series of non-concentrating cycles, in which both exit and inlet $pCO_2$ were 0.47 bar, utilizing a DSPZ-based flow cell at 40–150 mA $cm^{-2}$.[18] In the present work we show the use of this setup for $CO_2$ separation from low partial pressure in a mixture with nitrogen and release into a pure $CO_2$ exit stream at 1.0 bar. **Fig. 2** demonstrates one such cycle with $pCO_2$ = 1.0 and 0.1 bar at the exit and inlet, respectively. Beginning at state $3'_i$, the upstream $CO_2$ partial pressure was set to 0.1 bar, which is close to its value in the flue gas from coal fired power plants.[7] We define $t$ as the time elapsed. As deacidification began (**Fig. 2a** and **b**, $t$ = 0.2 hr), the TA went up at a linear rate because only $K^+$ ions crossed the cation exchange membrane (CEM) when a constant 40 mA $cm^{-2}$ current density was applied (**Fig. 2c**).[18] As a result of the PCET reactions during the reduction of DSPZ, the negolyte pH (**Fig. 2d**) increased from near neutral to ~13.5 at the end of the deacidification process, indicated by the steep increase of voltage until reaching the preset voltage cutoff of 1.65 V (**Fig. 2b**, $t$ = 0.6 hr). $CO_2$ invasion began when deacidification began but continued beyond the end of deacidification: invasion lasted until $t$ = 1.8 hr, as indicated by the $pCO_2$ signal returning to the 0.1 bar baseline, because of the limited reaction rate between dilute $OH^-$ and $CO_2$. The deviation in the gas flow rate (**Fig. 2g**) from the baseline starting at $t$ = 0.2 hr and returning at 1.8 hr also documents the complete capture process. As $CO_2$ reacted with hydroxide and water to form $CO_3^{2-}$ and $HCO_3^-$, the pH (**Fig. 2d**) dropped from ~13.5 at $t$ = 0.5 hr to 8.1 at 1.8 hr and then plateaued, once again indicating the completion of the capture process. The absorbed volume of $CO_2$ is 47 mL (eq. 1 in Methods). Assuming $T$ = 293 K, $p$ = 1 bar and ideal gas behavior, this absorption causes a change in DIC of 0.20 M (2.0 mmol $CO_2$ in 10 mL negolyte volume). We denote this change as $\Delta DIC_{flow,3'i\rightarrow1}$, where the subscript "*flow*" indicates that the value is measured by the downstream flowmeter and $CO_2$ sensor and "*3'i→1*" indicates that this value corresponds to the change in process $3'_i \rightarrow 1$ (**Table 1**). The same naming convention is used for both ΔTA and ΔDIC throughout the rest of this text. Unlike the flowmeter and $CO_2$ sensor, which quantify ΔDIC, the pH probe, in addition to providing a measured value ($pH_{meas}$), provides a direct measurement of DIC, because given two values from TA, DIC, $pCO_2$ and pH, the others can be derived.[18,21] At state $3'_i$, the DIC (regardless of subscripts) and TA values are calculated using $pH_{meas}$ and assumed gas-solution equilibrium, i.e. $CO_2(aq) = 0.035 \times pCO_2$, where 0.035 comes from Henry's law constant of 35 mM $bar^{-1}$ for $CO_2$ at room temperature. Because $\Delta TA_{3'i\rightarrow1}$ is known from **Fig. 2c**, $TA_1$ can be evaluated, and so can the TA values at other states. One way of obtaining DIC in all states except $3'_i$ and of obtaining ΔDIC values between all states is to use the known TA and $CO_2$(aq), and we denote these values with subscript "TA–eq" (**Table 1**). This method is also used to construct the ideal cycles [**ESI, Fig. S1**]. Another way to calculate DIC is to use the TA and $pH_{meas}$ without assuming gas-solution equilibrium. We denote DIC and ΔDIC calculated this way with subscript "TA–pH". The ΔDIC between state $3'_i$ and 1, i.e. 0.20 M, determined by flow meter and $CO_2$ sensor, i.e. $\Delta DIC_{flow,3'i\rightarrow1}$, is corroborated by $\Delta DIC_{TA-pH,3'i\rightarrow1}$ and $\Delta DIC_{TA-eq,3'i\rightarrow1}$ (**Table 1**).

**Table 1| Summary of TA, $pCO_2$, pH, DIC and ΔDIC.** TA is calculated by counting charges and assuming $K^+$ is the only ion passing through the CEM; $pCO_2$ is the $CO_2$ partial pressure at each state; $pH_{meas}$ refers to the negolyte pH measured by the pH probe. All DIC and TA values at state $3'_i$ are calculated using the measured pH and assuming gas-solution equilibrium. In all other states, $pH_{TA-eq}$ and $DIC_{TA-eq}$ are calculated using TA and assuming gas-solution equilibrium. $DIC_{TA-pH}$ is calculated using TA and $pH_{meas}$; $\Delta DIC_{TA-pH}$ and $\Delta DIC_{TA-eq}$ are the difference in $DIC_{TA-pH}$ and

$DIC_{TA-eq}$ values, respectively, between two consecutive states; $\Delta DIC_{flow}$ is converted from the volume of $CO_2$ captured or released, measured by the downstream flow meter and $CO_2$ sensor and $DIC_{flow}$ is calculated by adding $\Delta DIC_{flow}$ at the current state to $DIC_{flow}$ at the state one row above. Because $\Delta DIC_{flow}$ is not measurable between states 1 and 1' and states 3 and 3'$_f$, $DIC_{flow}$ at states 1' and 3'$_f$ is calculated by adding $DIC_{flow}$ with $\Delta DIC_{TA-pH}$ values between the corresponding states.

| State | TA (M) | $p_1$,$pCO_2$ (bar) | $pH_{meas}$ | $pH_{TA-eq}$ | $DIC_{flow}$ (M) | $DIC_{TA-pH}$ (M) | $DIC_{TA-eq}$ (M) | $\Delta DIC_{flow}$ (M) | $\Delta DIC_{TA-pH}$ (M) | $\Delta DIC_{TA-eq}$ (M) |
|---|---|---|---|---|---|---|---|---|---|---|
| 3'$_i$ | 0.11[a] | 0.1 | 7.4 | 7.4[a] | 0.11[a] | 0.11[a] | 0.11[a] | | | |
| | | | | | | | | 0.20 | 0.20 | 0.20 |
| 1 | 0.32 | 0.1 | 8.1 | 7.9 | 0.31 | 0.31 | 0.31 | | | |
| | | | | | | | | N/A | 0.03 | 0.03 |
| 1' | 0.32 | 1.0 | 7.1 | 6.9 | 0.34[b] | 0.34 | 0.34 | | | |
| | | | | | | | | 0.20 | –0.20 | –0.20 |
| 3 | 0.12 | 1.0 | 6.6 | 6.5 | 0.14 | 0.14 | 0.14 | | | |
| | | | | | | | | N/A | –0.03 | –0.03 |
| 3'$_f$ | 0.12 | 0.1 | 7.5 | 7.5 | 0.12[c] | 0.12 | 0.12 | | | |

[a] All values derived from $pH_{meas}$, assuming gas-solution equilibrium
[b] Calculated by summing $DIC_{flow,1}$ and $\Delta DIC_{TA-pH,1-1'}$
[c] Calculated by summing $DIC_{flow,3}$ and $\Delta DIC_{TA-pH,3-3'f}$

After $CO_2$ capture at 0.1 bar ($p_1$) was completed, the headspace of the negolyte was switched to a pure $CO_2$ environment ($p_3$) to prepare for $CO_2$ outgassing, i.e. going through process 1→1' (**Fig. 2e,** $t$ = 2.2 hr**)**. The drop in flow rate at $t$ = 2.2 hr and its return to the baseline at 2.5 hr is caused by the combined effect of mismatched valve response rate in the MFCs (the $N_2$ MFC valve closes faster than the $CO_2$ MFC valve opens) and a small increase in DIC due to increased $pCO_2$ in the headspace. This increase in DIC, corresponding to $\Delta DIC_{1\rightarrow1'}$, is difficult to quantify via the flowmeter and $CO_2$ sensor, but can be determined using $pH_{meas}$ ($\Delta DIC_{TA-pH,1\rightarrow1'}$) or assuming gas-solution equilibrium ($\Delta DIC_{TA-eq,1\rightarrow1'}$), which both give 0.03 M (**Table 1**). The acidification+$CO_2$ outgassing (process 1'→3) started at $t$ = 3.2 hr and ended at a little over 3.6 hr (**Fig. 2a-d** and **g**). Note that, unlike in process 3'$_i$→1, the $CO_2$ outgassing, which is observable from pH change and an increase in flow rate, (**Fig. 2d** and **g)** lasted for no more than ten minutes after the acidification process (**Fig. 2a** and **b**) finished. The outgassed $CO_2$ volume was 49 mL (eq. 1), which is equivalent to $\Delta DIC_{flow,1'\rightarrow3}$ = –0.20 M. Once again, $\Delta DIC_{TA-pH}$ and $\Delta DIC_{TA-eq}$ agree with $\Delta DIC_{flow}$ for the changes between states 1' and 3. Starting from a little over $t$ = 5.2 hr, the headspace was filled with 0.1 bar $CO_2$ + 0.9 bar $N_2$ to recover the state 3' for the next cycle (process 3→3'$_f$). Like process 1→1', there was a combined effect of valve response and additional $CO_2$ outgassing during process 3→3'$_f$, causing an increase in flow rate (**Fig. 2g**, $t$ = 5.2 hr to 5.6 hr). Note that state 3'$_f$ has slightly higher pH and 0.01 M more of TA and DIC than state 3'$_i$ because of the influence of oxygen (**Fig. 1c**).

## Calculation of $\Delta DIC_{flow,3\rightarrow1}$ ,Molar Cycle Work and Productivity

The discussion above shows how $\Delta DIC_{flow,3'i\rightarrow1}$ and $\Delta DIC_{flow,1'\rightarrow3}$ are obtained by gas flow measurement, but neither of these two quantities reflect the actual amount captured at 0.1 bar and released at 1.0 bar, because both states 3'$_i$ and 1 are at $p_1$ = 0.1 bar while both states 1' and 3 are at $p_3$ = 1 bar. The important quantity is the difference in DIC between states 3 and 1. With help of TA and pH measurements, $\Delta DIC_{flow,1\rightarrow3}$ is evaluated as $\Delta DIC_{TA-pH,1\rightarrow1'} + \Delta DIC_{flow,1'\rightarrow3}$ = –0.17 M; equivalently, but with opposite sign, $\Delta DIC_{flow,3\rightarrow1} = \Delta DIC_{flow,3'\rightarrow1} + \Delta DIC_{TA-pH,\,3\rightarrow3'f}$ = 0.17 M, i.e., 1.7 mmol $CO_2$ in a 10 mL negolyte volume. Because sufficient gas-solution equilibrium is

approached (**Fig. 2f** and **g)**, $\Delta DIC_{TA-eq}$ may also be used in place of $\Delta DIC_{TA-pH}$ in such calculations, resulting in the same values of $\Delta DIC_{flow,1\rightarrow3}$ and $\Delta DIC_{flow,3\rightarrow1}$.

In this cycle, the deacidification work into the system, $w_{deacidification}$, is 0.267 kJ and the acidification work, $w_{acidification}$, is –0.119 kJ (eq. 3). Dividing the cycle work, $w_{cycle}$ (eq. 2), by 1.7 mmol $CO_2$ gives the molar cycle work of 87 kJ $mol_{CO2}^{-1}$. This value is already competitive with commercial amine scrubbing processes,[4,6] and it can be further decreased by using membranes with lower ohmic resistance or molecules with lower electron transfer overpotential.[22]

The productivity measures the rate of a $CO_2$ separation process and may be evaluated by dividing $\Delta DIC_{flow,3\rightarrow1}$, i.e. 0.17 M, by the sum of the absorption time and the desorption time. The $CO_2$ absorption and desorption processes took 1.6 and 0.4 hr, respectively, leading to a productivity of 0.085 M $hr^{-1}$ or $8.5 \times 10^{-4}$ $mol_{CO2}$ $hr^{-1}$. The productivity should vary monotonically with current density because the desorption process is mostly limited by the rate of TA consumption, which is proportional to the rate of electrochemical oxidation. The solution-gas contacting area is quite limited in this experiment: gas was simply bubbled through the solution at a low rate (11.8 mL/min). Engineered contactor structures have many orders of magnitude higher contact area. Because the sorbent in this process is aqueous KOH, the contactor that is used for the concentrated alkaline process [9] might be adopted, for example, and a similar capture rate would be expected. Other factors such as solution concentration, gas flow rate, etc. also influence the productivity but analysis of such dependencies is beyond the scope of this study.

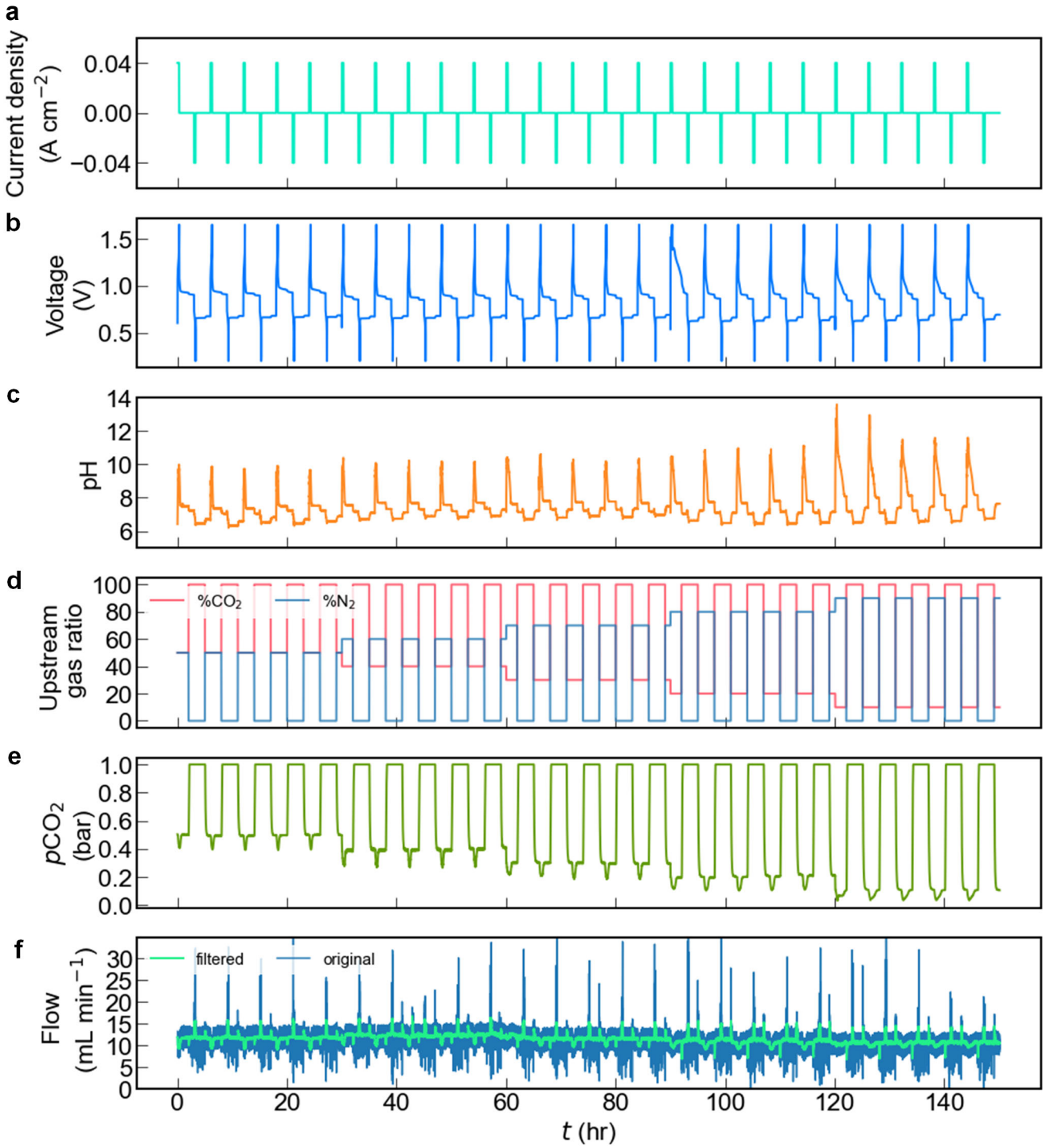


**Fig. 3| Twenty five $CO_2$ concentrating cycles with 0.5, 0.4, 0.3, 0.2, and 0.1 bar inlet $pCO_2$ and 1 bar exit $pCO_2$ at 40 mA cm$^{-2}$.** Same cell and negolyte as in **Fig. 2** were employed**. a**, Current density. **b**, Voltage. **c**, pH of the negolyte. **d**, $N_2$ and $CO_2$ percentage in the upstream source gas, controlled by mass flow controllers; total pressure 1.0 bar. **e**, downstream $CO_2$ partial pressure. **f**, downstream total gas flow rate.

**Carbon Capture Cycles with $p_1$ = 0.1 – 0.5 bar at 40 mA cm$^{-2}$**

In order to understand how the electrical work depends on the inlet $pCO_2$, we performed five cycles each at $p_1$ = 0.1 to 0.5 bar with $p_3$ = 1.0 bar (**Fig. 3**). The same cell components and negolyte as in **Fig. 2** were used, and the posolyte was replaced with a fresh solution for each inlet condition to avoid oxygen-induced long-term cell imbalance (**Fig. 1c**).[23] **Fig S5b** shows that the $CO_2$ outgassing period is identical regardless of inlet $pCO_2$ because the exit $pCO_2$ is always 1 bar and the current density is always 40 mA cm$^{-2}$. In contrast, the capture period increases as inlet $pCO_2$ decreases (**ESI**, **Fig S5a**) because of the expected trend of reaction rate with decreasing reactant concentration. $\Delta DIC_{flow,3\rightarrow1}$ values decrease as $p_1$ decreases (**Fig. 4a**) because of greater $\Delta DIC$ during processes 1→1' and 3→3' (vertical arrows in **Fig. 4c**) at smaller $p_1$. The measured values closely align with the theoretical $\Delta DIC_{TA-eq,3\rightarrow1}$ vs. $p_1$ curve (**Fig. 4a**).

This alignment permits us to estimate $\Delta DIC_{flow,3\rightarrow1}$ for $p_1$ = 0.4 mbar and $p_3$ = 1 bar, i.e. similar to DAC conditions, by following the $\Delta DIC_{TA-eq,3\rightarrow1}$ vs. $p_1$ curve to obtain a value of 0.049 M. Note that the $\Delta DIC_{TA-eq,\,3\rightarrow1}$ vs. $p_1$ curve shifts downward as $TA_{3'i}$ increases (**ESI**, **Fig. S3b**). This has relatively small impacts on $\Delta DIC_{TA-eq,3\rightarrow1}$ with high $p_1$, but it causes significant differences for small $p_1$ values. For example, when $p_1$ = 0.4 mbar, $\Delta DIC_{TA-eq,3\rightarrow1}$ for $TA_{3'i}$ = 0, 0.11 and 0.21 M is 0.097, 0.049 and 0.005 M, respectively (**ESI**, **Fig. S1-3**). Because $\Delta DIC_{3\rightarrow1}$ is in the denominator when $CO_2$ molar cycle work is calculated, lowering $\Delta DIC_{3\rightarrow1}$ increases the molar energy cost accordingly (**ESI**, **Fig. S2b** and **c**). High $TA_{3'i}$ should therefore be avoided, and a necessary step to achieve this goal is to limit the impact of oxidation of $DSPZH_2$ by oxygen (**Fig. 1c**).

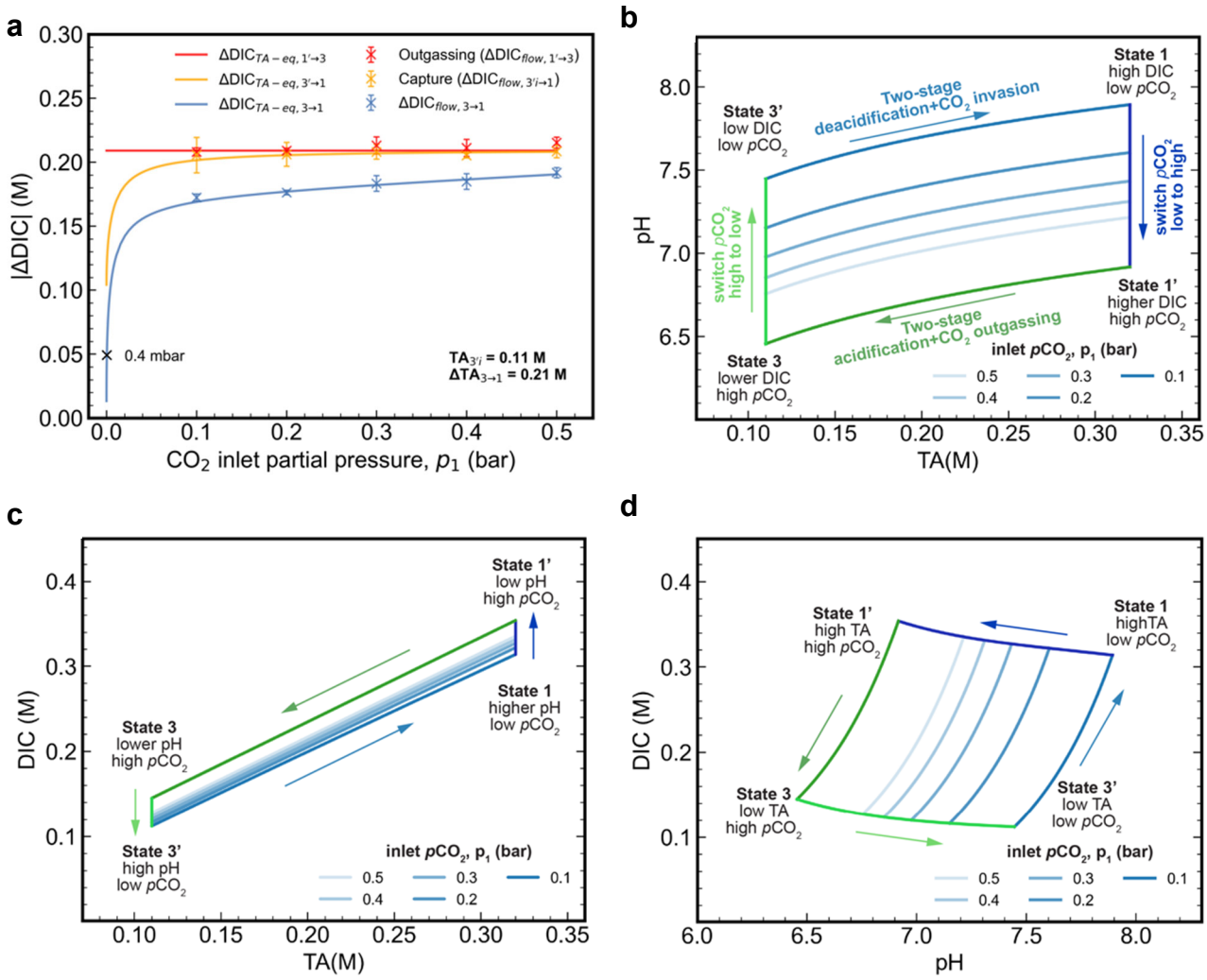


**Fig. 4| Summary of the experimental concentrating cycles with different inlet $pCO_2$ in Fig. 3 and the TA/pH/DIC relations of the ideal cycles with corresponding experimental conditions. a**, $\Delta DIC_{flow}$ extracted from **Fig. 3 e** and **f** (colored "x" markers) and calculated $\Delta DIC_{TA-eq}$ given $TA_{3'i}$ = 0.11 M and $\Delta TA_{3\rightarrow1}$ = 0.21 M (lines). The black "x" marker refers to the result that ΔDIC for the ideal cycle equals 0.049 M when $pCO_2$ = 0.4 mbar. **b**, pH *vs.* TA in the ideal cycles, assuming $TA_{3'i}$ = 0.11 M, $\Delta TA_{3\rightarrow1}$ = 0.21 M and gas-solution equilibrium. $p_1$ in the legends represents $pCO_2$ during the two-stage deacidification+$CO_2$ invasion process. The arrows indicate the direction of the processes in the experiments. **c**, DIC *vs.* TA in the ideal cycles. **d**, DIC *vs.* pH in the ideal cycles.

**Carbon Capture Cycles with $p_1$ = 0.1 – 0.5 bar at 20 – 150 mA cm$^{-2}$**

The average $CO_2$ molar cycle work under 40 mA cm$^{-2}$ is compared with those obtained under 20 −150 mA cm$^{-2}$ (**Fig. 5 a** and **ESI**, **Fig. S7**). As current density increases at a fixed $p_1$, the net cycle work increases as the required deacidification work increases and the acidification work returned decreases in magnitude; these trends are caused by increased ohmic, electron-transfer and mass-transport overpotentials at higher current density.[22] It is noteworthy that we achieve 61.3 kJ mol$_{CO2}^{-1}$ cycle work for $p_1$= 0.1 bar and $p_3$ = 1 bar using a current density of 20 mA cm$^{-2}$, which is a competitive energy cost at a much higher current density compared to other electrochemical $CO_2$ separation methods for flue gas capture.[24,25].

It is evident from **Fig. 5b** that $\Delta DIC_{flow,3\rightarrow1}$ is independent of current density for a given value of $p_1$. This occurs because varying current density changes only the rate of change in TA and not the value of $\Delta TA_{3\rightarrow1}$, and sufficient reaction time was allowed to approach gas-solution equilibrium, whether the current density was low (**Fig. 2f** and **g**) or high (**ESI**, **Fig. S9)**. The consistent $\Delta TA_{3\rightarrow1}$ across various current densities is supported by the consistent charge/discharge capacities (**ESI**, **Fig. S8)**. The slight variations in ΔTA and ΔDIC were caused by occasional foaming or negolyte droplets clinging to the wall of the reservoir, both of which cause small amounts of charge capacity to be instantaneously inaccessible from time to time. In contrast, increasing $pCO_2$ at the inlet raises $\Delta DIC_{flow,3\rightarrow1}$ (**Fig. 5b**), for the reason explained in the discussion of Fig. 4d. In addition to the cycle results presented in **Fig. 5**, five cycles with $p_1$ = 0.05 bar and $p_3$ = 1 bar and current density being 40 mA cm$^{-2}$ were tested under faster negolyte pumping to enhance mass transport rates, yielding an average cycle work of 92.6 kJ mol$_{CO2}^{-1}$(**ESI**, **Fig. S10**).

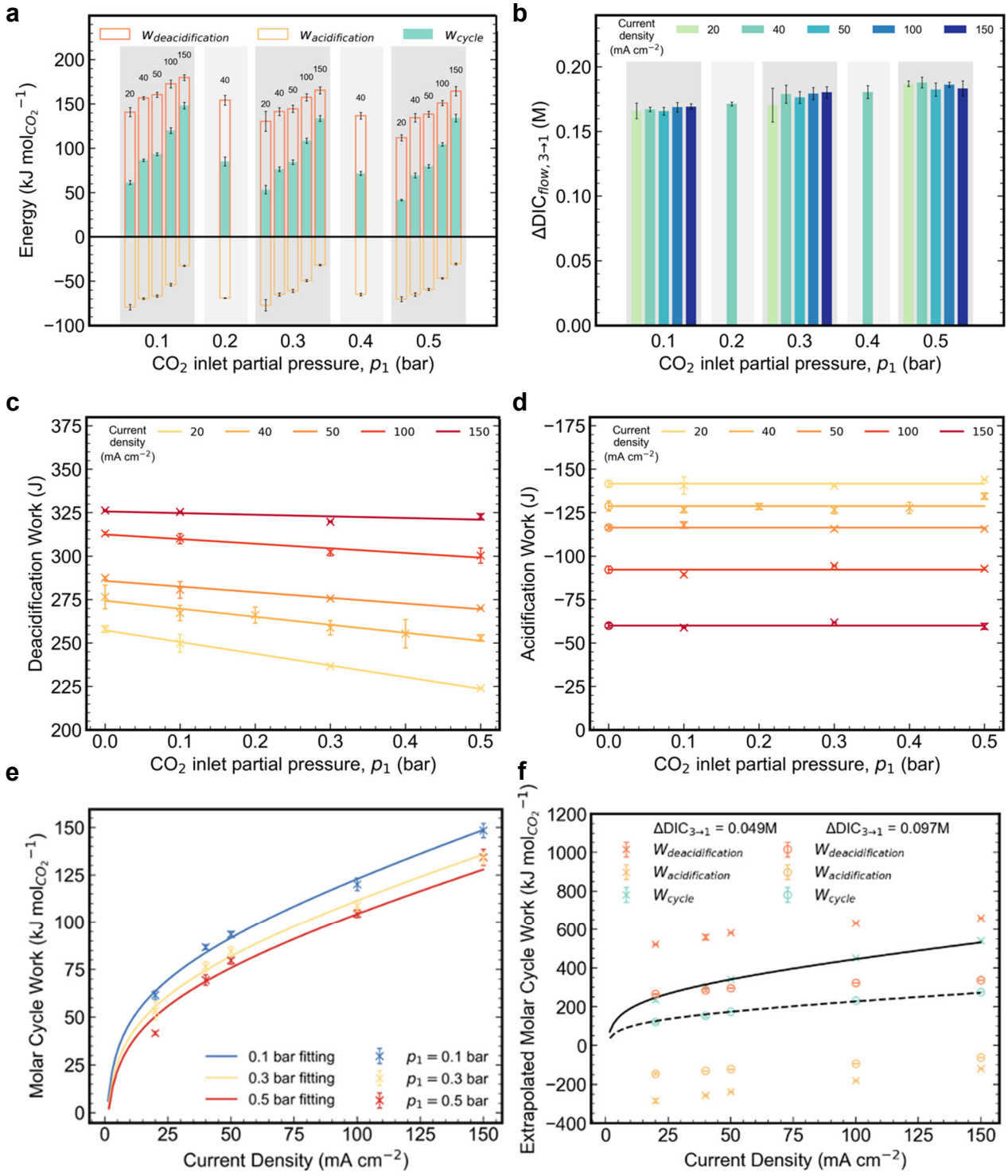


**Fig. 5| Summary of the experimental concentrating cycles performed under 20, 40, 50, 100 and 150 mA $cm^{-2}$ current densities and $p_1$ = 0.5, 0.4, 0.3, 0.2 and 0.1 bar.** Electrolytes comprised 10 mL of 0.11 M DSPZ in 1 M KCl (negolyte) and 35 mL of 0.1 M $K_4Fe(CN)_6$ and 0.04 M $K_3Fe(CN)_6$ in 1 M KCl (posolyte). The error bars refer to standard deviation. **a**, $CO_2$ molar deacidification, acidification and cycle work *vs.* $p_1$ for current densities indicated above the bars, in mA $cm^{-2}$. In both **a** and **b** the horizontal axis is categorical, and each shadowed region refers to a single $p_1$ value. **b**, $\Delta DIC_{flow,3\to1}$ *vs* $p_1$ for various current densities. **c**, Deacidification work *vs.* $p_1$ for various current densities. The "x" markers refer to measured data. The deacidification work of the cycles under pure $N_2$ is used for $p_1$ = 0.0 bar. **d**, Acidification work *vs.* $p_1$ for various current densities. The "x" markers refer to measured data. For each current density,

the acidification work at $p_1$ = 0.0 bar ("o" markers) is chosen to be the average value of the work obtained at other $p_1$ values at the same current density. **e**, $CO_2$ molar deacidification, acidification and cycle work vs. current density for $p_1$ = 0.1, 0.3 and 0.5 bar. The curves are fitted using a Tafel model. **f**, Extrapolated $CO_2$ molar deacidification, acidification and cycle work for $p_1$ = 0.4 mbar. Extrapolation is performed using deacidification and acidification work at 0.0 bar $p_1$ in **c** and **d**, and divided by $\Delta DIC_{TA\text{-}eq,3\rightarrow1}$ at $p_1$ = 0.4 mbar obtained from **Fig. 4a** and **Fig. S2b**. The solid line refers to a Tafel model fit of $CO_2$ molar cycle work *vs.* current density assuming $TA_{3'i}$ = 0.11 M ($\Delta DIC_{3\rightarrow1}$ = 0.049 M) and the dashed line refers to the same fitting but assuming $TA_{3'i}$ = 0.0 M ($\Delta DIC_{3\rightarrow1}$ = 0.097 M).

## Estimate of Molar Cycle Work at $p_1$ = 0.4 mbar and $p_3$ = 1 bar

Because of the limited sensitivity of our equipment, a direct measurement of $CO_2$ molar cycle work at $p_1$ = 400 ppm and $p_3$ = 1 bar, i.e. similar to DAC conditions, is currently infeasible in our laboratory, but we can extrapolate the molar cycle work under these conditions using the results obtained from $p_1$ = 0.1 – 0.5 bar. However, a simple linear regression of the molar cycle work from higher $p_1$ values to $p_1$ = 0.4 mbar does not guarantee accurate extrapolation because the deacidification work (**Fig. 5c**), i.e. part of the numerator in the calculation of molar cycle work (eq. 2-4 in the method section), scales linearly with $p_1$, whereas $\Delta DIC_{flow,3\rightarrow1}$, i.e. part of the denominator in the calculation of molar cycle work (eq. 4 in the method section), scales non-linearly with $p_1$ (**Fig. 4a** and **d, Fig. S 3b**). Therefore, we evaluate the molar cycle work at $p_1$ = 0.4 mbar by separately calculating $\Delta DIC_{flow,3\rightarrow1}$ and the cycle work (i.e. the sum of the experimental deacidification work (**Fig. 5c**) and the acidification work (**Fig. 5d**)). The deacidification work at $p_1$ = 0.4 mbar is simply approximated by the deacidification work under a pure $N_2$ atmosphere, i.e. 0.0 bar $pCO_2$ (**Fig. 5c**); the reason that deacidification work decreases with increasing $p_1$ is that increasing $p_1$ lowers the average negolyte pH, which in turn decreases the cell voltage and thereby decreases the work (eq. 3 in the method section). The acidification work is always the same regardless of $p_1$ because $p_3$ is always 1 bar and $\Delta TA_{3\rightarrow1}$ is always the same (hence the flat lines in **Fig. 5d**); therefore, for $p_1$= 0.0 bar we use the average acidification work from higher $p_1$ values. As for $\Delta DIC_{flow,3\rightarrow1}$ at $p_1$ = 0.4 mbar, we assume it is equal to the value of $\Delta DIC_{TA\text{-}eq,3\rightarrow1}$ in the ideal cycle at the same pressure. We have shown that measured ($\Delta DIC_{flow,3\rightarrow1}$) and ideal cycle ($\Delta DIC_{TA\text{-}eq,3\rightarrow1}$) values of $\Delta DIC_{3\rightarrow1}$ at $p_1$= 0.1 – 0.5 bar agree very well (**Fig. 4a**, blue curve). With $TA_{3'i}$ = 0.11 M and $\Delta TA_{3\rightarrow1}$ = 0.21 M, the ideal cycle value of $\Delta DIC_{TA\text{-}eq,3\rightarrow1}$ at $p_1$ = 0.4 mbar and $p_3$ =1 bar is 0.049 M (**Fig. 4a**, **Fig. S 2b**). The molar cycle work for various current densities, evaluated by dividing the sum of deacidification and acidification work at $p_1$= 0.0 bar by $\Delta DIC_{TA\text{-}eq,3\rightarrow1}$ of 0.049 M, is shown in **Fig. 5f**. **Fig. 5f** suggests that the molar cycle work at 20 mA $cm^{-2}$ is 237.4 kJ $mol_{CO2}^{-1}$. This is on par with the concentrated KOH process.[9] However, if there is no initial alkalinity, i.e. $TA_{3'i}$ = 0.0 M, and the same $\Delta TA_{3\rightarrow1}$ = 0.21 M is kept, the cycle work may be cut in half to 122.4 kJ $mol_{CO2}^{-1}$; this occurs because of the nearly doubled $\Delta DIC_{flow,3\rightarrow1}$ of 0.097 M despite similar cycle work (**ESI**, **Fig. S2 and S3**). The non-linear molar cycle work trend was fitted with a Tafel model, which suggests 72.8 and 98.1 kJ $mol_{CO2}^{-1}$ at 5 and 10 mA $cm^{-2}$, respectively **(ESI, Non-Linear Fit of Molar Cycle Work With Tafel Model)**. In addition, due to its solubility of 0.7 M in aqueous solution,[18] DSPZ can induce a $\Delta TA_{3\rightarrow1}$ or $\Delta[OH^-]$ of 1.4 M and thereby potentially yield even lower molar cycle work (**ESI**, **Fig. S4**)

## Comparison with Existing Technologies

**Table 2** summarizes some of the emerging technologies for point source capture, DAC, and direct ocean capture (DOC), where $CO_2$ is removed from seawater, allowing more $CO_2$ uptake by the ocean. Many approaches to DAC have used aqueous alkaline solutions[2,9] or solid amine-based

adsorption methods,[2,24] which require thermal excursions to release captured $CO_2$. One of the state-of-the-art DAC approaches relies on concentrated (2-5 Molar) alkaline solutions on a high-area contactor to absorb $CO_2$ and transform it into aqueous $K_2CO_3$ and $KHCO_3$. These are then converted into solid $CaCO_3$ in a pellet reactor by mixing the aqueous carbonates with $Ca(OH)_2$. Releasing the $CO_2$ requires heating the $CaCO_3$ to 900 °C in an oxygen-fired calciner, which costs 264-296 kJ/mol$CO_2$.[2,9] Another, less mature, aqueous approach uses amino acids for the carbon capture step and undergoes a subsequent sorbent regeneration cycle employing solid bis-iminoguanidine carbonate precipitation and $CO_2$ release through heating to >100 °C; this cycle requires 152-422 kJ/mol$CO_2$, depending on the type of guanidine, because a significant portion of the energy contributes to removing the undesirable hydrate from guanidine carbonate crystal.[10,16] Solid sorbent DAC, mostly based on solid amine absorption and release through thermal and/or pressure swing, allows reduced heating requirements (~100 °C), but amine decomposition may lead to high operational and end-of-life costs.[2,26-28]

Electrochemical carbon capture methods may offer solutions to overcome the high sorbent regeneration energy penalty and sorbent decomposition issues. Electrochemically mediated point source carbon capture methods[7,24,29], at low current densities, have exhibited lower energetic costs than amine-scrubbing methods. In addition, $CO_2$ removal from ocean water, which restores the $CO_2$ capture capability of oceans, via electrochemical methods such as bipolar membrane electrodialysis (BPMED), have shown promisingly low energetic cost.[12,13] However, the demonstrated works exhibited either low current density (slow kinetics) or low voltage efficiency. In addition, the high water-handling requirement of direct ocean capture adds significantly to the energetic cost.

The performance of our pH-swing flow cell, demonstrated for capture at 0.1 bar and projected for 0.4 mbar appears competitive compared with existing technologies, not only in terms of energetic cost with cheap electricity from renewable sources, but also because of much larger applicable current density (**Table 2**).[30] Additionally, the all-liquid configuration obviates the need for the precipitation and heating of solid carbonates. Furthermore, the compatibility with an aqueous electrolyte of non-volatile, non-corrosive and potentially low-cost organic molecules implies that a carbon capture technology based on this concept has the potential for wide scale practical implementation.

**Table 2| Comparison of this work and emerging technologies for DAC, DOC and point source capture. $CO_2$ separation work with "th" subscript denote thermal energy inputs, whereas "e" subscript denotes electrical work input.**

| Method | Purpose | $CO_2$ separation work inputs (kJ $mol_{CO2}^{-1}$) | Current Density (mA $cm^{-2}$) |
|---|---|---|---|
| Alkaline solvent[2, 9] | DAC | $264\text{-}396_{th}$[a] | N/A |
| Solid amine sorbents[2] | DAC | $150 - 211_{th}$[b] | N/A |
| Amino acid solvents and solid bis-iminoguanidines[10] | DAC | $152 - 422_{th}$[c] | N/A |
| Fuel cell concentrator[17] | DAC | $350_e$[d] | 0.5 |
| Electrochemical alkaline sorbent regeneration [31] | DAC | $374_e$[f] | 0.5 |

| | | | |
|---|---|---|---|
| Processing seawater within a BPMED reactor[13] | DOC | $155_e$[g] | 3.3 |
| Titrating seawater with BPMED acid/base[12] | DOC | $394_e$[h] | 100 |
| Traditional amine ab-/desorption[4] | Point source capture | $132 – 150_{th}$ | N/A |
| Amine ad-/desorption with advanced flash stripper[32] | Point source capture | $92_{th}$[i] | N/A |
| Shell Cansolv[6] | Point source capture | $103_{th}$ | N/A |
| Petra Nova[33] | Point source capture | $89_{th}$[j] | N/A |
| Quinone Direct binding[7] | Point source capture | $56_e$[k] | 0.5 |
| EMAR[8] | Point source capture | $30 – 113_e$[l] | 2.7 – 11.8 |
| ***This work*** | 0.1 bar capture | **$61 – 145_e$** | **20 – 150** |
| | 0.4 mbar capture | **$121\text{-}237_e$** | **20 (extrapolated)** |

[a]Work input excludes electrical work required to operate air-liquid contactor, pellet reactor and auxiliary equipment.
[b]Desorption energy for mid-range scenario; work input excludes electrical work required to operate air contactor fans and desorption vacuum pump.
[c]Energy required for bis(iminoguanidine) regeneration.
[d]Hydrogen gas is the energy source; Energy required to operate water cooling system is excluded.
[f]The process starts with a bicarbonate/carbonate solution, mimicking a solution saturated with DIC under 0.4 mbar inlet $pCO_2$. The value is the required work for alkaline sorbent solution regeneration.
[g]Work input excludes costs for ocean water intake, pre-treatment and pumping.
[h]Energy consumption for the best-case acid process; Work input excludes electrical work required to operate pumps and chiller.
[i]The inlet gas source contains 11.3% $CO_2$, and the exit is 99% $CO_2$.
[j]The inlet gas source contains 11% $CO_2$, and the exit is 97% $CO_2$. This energy is calculated using the electrical power cost, excluding 50% used for compression, plus the steam cost associated with the CCS plant. The captured $CO_2$ was offset by the $CO_2$ emission in the CCS plant.
[k]The inlet gas source was simulated flue gas with 15% $CO_2$ and 3% $O_2$ in $N_2$, and exit partial pressure was ~0 bar. Note that the energy cost was calculated based on the amount of $CO_2$ absorbed, yet it is not clear that all absorbed $CO_2$ was released.
[l]Energy and current density values adopted from Fig.8(a) of ref.[8] Simulated flue gas is 15% $CO_2$ in $N_2$.

## Electrochemical Rebalancing

It is clearly difficult to avoid $O_2$ in either DAC or flue gas capture because the source gas contains 20% and 3–5% $O_2$, respectively. In the short term, the oxidation of $DSPZH_2$ by $O_2$ incurs an instantaneous loss in Coulombic efficiency. In the long term the cell will go out of balance, accumulating oxidized species in both electrolytes and $TA_{3^-i}$, KOH and $DIC_{3^-i}$ in the negolyte (**Fig. 1c**).[23] As a result, $\Delta DIC_{3\rightarrow1}$ will shrink without a concomitant decrease in cycle work (**ESI**, **Fig. S2b**), leading to an increase in $CO_2$ molar cycle work (**ESI**, **Fig. S2c**). Eventually the cell will no longer operate because both electrolytes are completely oxidized. As shown in **Fig. 6a** and **b**, as soon as the headspace was opened to air the Coulombic efficiency decreased to ~65%, and by the 20$^{th}$ subsequent cycle the cell lost all capacity due to depletion of reduced species, i.e. $[K^+]_4[Fe^{II}(CN)_6]^{4-}$, in the posolyte side. The negolyte pH also increased from near neutral to almost 14 during air exposure (**ESI**, **Fig. S14b**). Development of oxygen-insensitive molecules may

alleviate the problem caused by oxygen, but even if a tiny amount of Coulombic efficiency loss, e.g. 0.1%, took place every cycle, the effect is cumulative and will eventually lead to an out-of-balance cell problem (**Fig. 1c**).

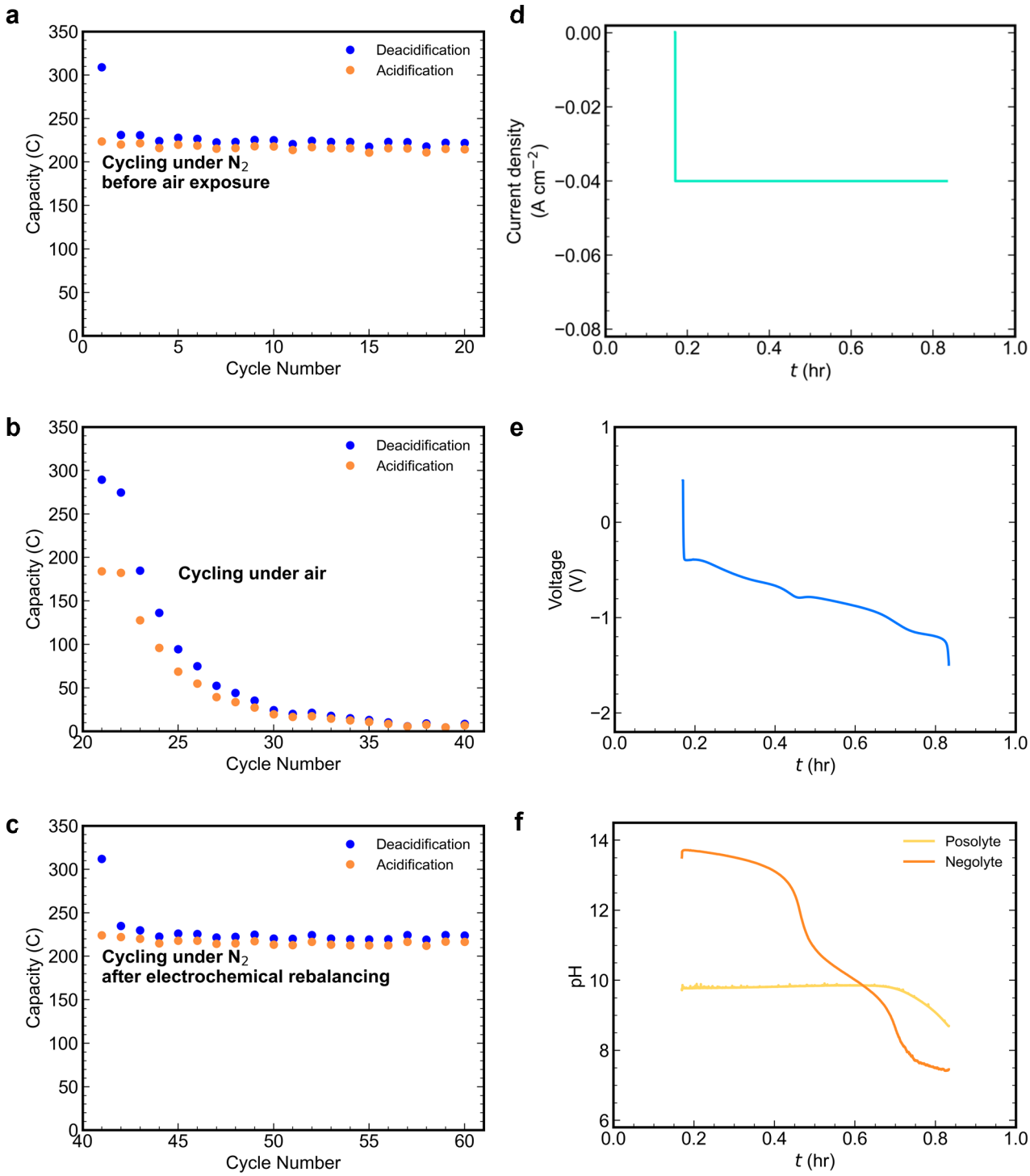


**Fig. 6| The capacity fade caused by $O_2$ on $Fe(CN)_6$|DSPZ cell cycling (a,b,c) and its mitigation by the electrochemical rebalancing method (d,e,f). a**, Charge capacity *vs.* cycle number of the cell under pure $N_2$ atmosphere. The first cycle has much higher deacidification capacity due to residual oxygen **b**, Charge capacity *vs.*

cycle number of the same cell from **a** under air. Capacity fades quickly because of the depletion of $K_4Fe(CN)_6$ in the posolyte. **c**, Charge capacity *vs*. cycle number of the cell from **b** under pure $N_2$ atmosphere, after the electrochemical rebalancing step. The first cycle has much higher deacidification capacity due to residual oxygen. **d**, Current density, **e**, voltage, **f**, Posolyte and negolyte pH during the electrochemical rebalancing step

Here we demonstrate the efficacy of the electrochemical rebalancing method. The method successfully recovers the pH of the negolyte and the capacity of the cell, which is thrown out-of-balance by $O_2$-induced side reactions. The electrochemical rebalancing process comprises the cathodic reaction $[K^+]_3[Fe^{III}(CN)_6]^{3-} + e^- \rightarrow [K^+]_4[Fe^{II}(CN)_6]^{4-}$ in the posolyte and the anodic oxygen evolution reaction, $OH^- \rightarrow 2e^- + ½O_2$, in the negolyte. **Fig. 6d,e** and **f** show the cell behavior when the electrochemical rebalancing process is applied to the completely out-of-balance cell (**Fig. 6b**). The process starts when a constant current of $-40$ mA cm$^{-2}$ is applied (**Fig. 6d**). The voltage immediately drops from 0.2 V to negative values because both the cathodic and anodic half reactions are at ~0.4 V vs. SHE at pH 14, and there is high activation overpotential for the oxygen evolution reaction (**Fig. 6e)**. As the rebalancing process progresses, the pH of the negolyte side decreases (**Fig. 6f**), causing the anodic half reaction to shift to higher potential, thereby further decreasing the cell potential (**Fig. 6e**). The sharp drop in voltage to a plateau near 0.8 hours indicates the completion of the electrochemical rebalancing process. **Fig. 6c** shows the post-rebalancing cell capacity, which is almost identical to that prior to air exposure (**Fig. 6a**), indicating that essentially all lost capacity due to imbalance has been restored. The capacity accounting for all the electrons passed in the electrochemical rebalancing step is 476.8 C, which is within 1% of the theoretical capacity (473 C) of the posolyte side, suggesting a complete recovery of the $K_4Fe(CN)_6$ and minimal side reactions other than oxygen evolution. The posolyte pH did not change much during the process because the cathodic half-reaction is not proton-coupled (**Fig. 6f**). The neutral pH of the negolyte at the end of the process indicates that virtually all of the accumulated hydroxide has been removed (**Fig. 6f**). The undiminished capacity also suggests that this method is not detrimental to DSPZ. **Fig. S14** shows that the electrolytes, after electrochemical rebalancing, have the same carbon-capture capability as the original electrolytes, and the NMR spectra in **Fig. S15** suggest no new species was generated during the process. Hence, the electrochemical rebalancing process is a very effective method to remove the adverse effect of oxygen in DSPZ-based carbon capture flow cells. This method has potentially broad application beyond DSPZ and carbon capture, e.g. mitigating the oxygen effect in flow batteries with air or pH sensitive electrolytes **(ESI, More on Electrochemical Rebalancing**).[23,34-41] The overall energy cost is 378 J, which is approximately 1.4 times of the cost of one deacidification half cycle at 40 mA cm$^{-2}$ (**Fig. 5c**). This will be a significant cost if the electrochemical rebalancing is applied every few cycles, which may be necessary for a DSPZ-based system for DAC, but if the negolyte molecule is much less air sensitive or the source gas has lower oxygen content, requiring electrochemical rebalancing less frequently than once every few tens of carbon capture/release cycles, the cost will be negligible. The development of oxygen-insensitive molecules for this purpose is the subject of active research.

## Conclusion

In this work, we have performed a series of $CO_2$ concentrating cycles using a DSPZ-based flow cell with electrochemically induced pH swings, and the cycle work under different inlet partial pressures and current densities was analyzed and compared. We demonstrated a 61.3 kJ mol$_{CO2}^{-1}$ cycle work for $CO_2$ separation for capture at $p_1 = 0.1$ bar and release at $p_3 = 1$ bar, at a current

density of 20 mA $cm^{-2}$. If $TA_{3,i}$ is carefully maintained at a low level, the extrapolated separation work for $p_1$ = 0.4 mbar and $p_3$ = 1 bar is 121 kJ $mol_{CO2}^{-1}$ at 20 mA $cm^{-2}$ and this figure can be further lowered if a higher concentration of DSPZ or another PCET-active molecule is used. Our Tafel model suggests that molar cycle work at $p_1$ = 0.4 mbar may be even lower than 100 kJ $mol_{CO2}^{-1}$ at smaller current densities. Recognizing the inevitable $O_2$-induced imbalance and capacity fade in both point source capture and DAC, we report an electrochemical rebalancing method that recovers the initially healthy cell composition. This method can serve as a convenient tool for mitigating oxygen-related problems in many electrochemical applications. We anticipate that the low energetic cost of the pH swing cycles and the effectiveness of the oxygen mitigation method demonstrated here will accelerate the techno-economic competitiveness of electrochemically-driven carbon capture systems.

## Methods

### Materials and characterization

All chemicals were purchased from Sigma-Aldrich or Acros Organics and were used as received. The synthetic method for DSPZ is adapted from previous work.[18] In this work, sodium hydride was used to deprotonate the reaction intermediate phenazine-2,3-diol (DHPZ) instead of sodium methoxide (**Schematic S1**).

### Flow cell experiments

Flow cell experiments were constructed with cell hardware from Fuel Cell Tech. (Albuquerque, NM), assembled into a zero-gap flow cell configuration, similar to a previous report.[18] Pyrosealed POCO graphite flow plates with serpentine flow patterns were used for both electrodes. Each electrode comprised a 5 $cm^2$ geometric surface area covered by a stack of four sheets of Sigracet SGL 39AA porous carbon paper pre-baked in air for 24 h at 400 °C. The outer portion of the space between the electrodes was gasketed by Viton sheets with the area over the electrodes cut out. Torque applied during cell assembly was 80 lb-in on each of eight 1/4-28 bolts. The membrane used is a Fumasep E620(K) cation exchange membrane. Cell electrolytes comprised 10 mL 0.11 M DSPZ in 1 M KCl (negolyte, capacity limiting, theoretical capacity 212 C) and 35 mL 0.1 M $K_4Fe(CN)_6$ and 0.04 M $K_3Fe(CN)_6$ in 1 M KCl (posolyte, non-capacity limiting, theoretical capacity 473 C). For every new $CO_2$ capture cycle condition (changing current density or inlet $pCO_2$), the posolyte was replaced with a fresh solution and the negolyte was acidified by adding drops of 1 M HCl to remove the accumulating effect of oxygen side reactions. 10 µL of antifoam B emulsion purchased from Sigma-Aldrich was added into the negolyte solution before cell cycling to suppress foam formation. Posolytes were fed into the cell through fluorinated ethylene propylene (FEP) tubing at a rate of 100 mL $min^{-1}$ controlled by a Cole-Parmer 6 Masterflex L/S peristaltic pump, and the negolytes were circulated at the same rate controlled by a Cole-Parmer Masterflex digital benchtop gear pump system. Both posolyte and negolyte upstream gas was controlled by Sierra Smart Trak 50 Mass Flow Controllers. The flowmeter used in the downstream of negolyte headspace was a Servoflo FS4001-100-V-A. The $CO_2$ sensor was an ExplorIR-W 100% $CO_2$ sensor purchased from co2meter.com. A Mettler Toledo pH electrode LE422 was used to monitor electrolyte pH. As shown in **Fig. 1b**, a drierite drying tube (Cole Parmer) was placed in between the sensors and the negolyte chamber to reduce humidity level of the gas.

Glassy carbon (BASi MF-2012, 3.0mm diameter) was used as the working electrode for all three-electrode CV tests. A Ag/AgCl reference electrode (BASi MF-2052, pre-soaked in 3 M NaCl solution), and a graphite counter electrode were used for CV tests. CV tests and cell cycling were performed using a Gamry Reference 3000 potentiostat. All cycles were galvanostatic until the 1.65 V and 0.2 V voltage cutoff for deacidification and acidification, respectively, were reached, and then went through a potentiostatic process until the current reached 10 mA $cm^{-2}$. In the $CO_2$ cycles with $p_1$ = 0.1, 0.2, 0.3, 0.4, and 0.5 bar, the MFCs set the initial negolyte headspace atmosphere to be $p_1$, which was then switched back and forth between $p_1$ and $p_3$ every three hours. In the cycles with $p_1$ = 0.05 bar, the switching period was five hours.

**Calculation of absorbed or released $CO_2$ amount**

Because the deviation from baseline in **Fig. 2 g** is solely caused by $CO_2$ absorption, the amount of $CO_2$ captured is calculated by integrating over the difference between the recorded flow rate and the baseline in between 0.2 and 1.8 hours, i.e.

$$Q_{CO_2} = \sum_{n=t_i}^{t_f} (\dot{V}^{base} - \dot{V}^n)\Delta t \tag{1}$$

where $Q_{CO2}$ is the volume of $CO_2$, $t_i$ is the start time, $t_f$ is the final time, $\dot{V}^n$ is the instantaneous volumetric flow rate at $n^{th}$ data recording time $t_n$, $\dot{V}^{base}$ is the baseline flow rate of 11.6 mL $min^{-1}$, and $\Delta t$ is the time difference between successive measurements.

**Calculation of deacidification, acidification and cycle work**

The net cycle work is calculated by combining the work required for deacidification in process $3'_i \rightarrow 1$ and the work returned by acidification in process $1' \rightarrow 3$, i.e.

$$w_{cycle} = w_{deacidification} + w_{acidification} \tag{2}$$

The work in a process is calculated by summing over the product of voltage (**Fig. 2 a**) and current (**Fig. 2 b**), i.e.

$$w_{deacidification/acidification} = \sum_{n=t_i}^{t_f} V^n j^n A\, \Delta t \tag{3}$$

where $V^n$ is the cell voltage at the $n^{th}$ data recording time $t^n$, $j^n$ is the current density at $t^n$ and $A$ is the active geometric area of 5 $cm^2$.

The molar cycle work $\overline{w}$ is calculated by dividing $w_{cycle}$ by $-\Delta DIC_{flow,1\rightarrow 3}$ or $\Delta DIC_{flow,3\rightarrow 1}$:

$$\overline{w} = \frac{w_{cycle}}{\Delta DIC_{flow,3\rightarrow 1}} \tag{4}$$

where $\Delta DIC_{flow,1\rightarrow 3} = \Delta DIC_{TA-pH,1\rightarrow 1'} + \Delta DIC_{flow,1'\rightarrow 3}$ and $\Delta DIC_{flow,3\rightarrow 1} = \Delta DIC_{flow,3'\rightarrow 1} + \Delta DIC_{TA-pH,\ 3\rightarrow 3'f}$. For high current densities (100 and 150 mA $cm^{-2}$), we use $\Delta DIC_{TA-eq,1\rightarrow 1'}$ and $\Delta DIC_{TA-eq,\ 3\rightarrow 3'f}$ instead of $\Delta DIC_{TA-pH,1\rightarrow 1'}$ and $\Delta DIC_{TA-pH,\ 3\rightarrow 3'f}$, respectively, because of an artifact in the pH measurement at high current density, tentatively attributed to crosstalk between potentionstat lines. We explain in the main text that $\Delta DIC_{TA-pH}$ and $\Delta DIC_{TA-eq}$ are interchangeable when the pH measurement is valid.

**Data availability**: The data that support the plots and discussion of this study are available from the corresponding author upon reasonable request.

**Code availability**: The code that support the plots and discussion of this study are available from the corresponding author upon reasonable request.

## Conflicts of interest

None.

**Acknowledgments**

This research was supported by a grant from the Harvard University Climate Change Solutions Fund. We thank Daniel Schrag, Robert Gustafson, Anatoly Rinberg, Andrew Bergman, Tommy George and Eric Fell for helpful discussions.

**References**

[1]M.R. Raupach, G. Marland, P. Ciais, C. Le Quere, J.G. Canadell, G. Klepper, and C.B. Field, "Global and Regional Drivers of Accelerating $CO_2$ Emissions", *Proc Natl Acad Sci U S A* **104**, 10288 (2007).

[2]*Negative Emissions Technologies and Reliable Sequestration: A Research Agenda (2019)*. (The National Academies Press, 2019).

[3]"Annual Energy Outlook 2020 with Projections to 2050," edited by DOE (www.eia.gov/aeo, 2020).

[4]K. Goto, S. Kodama, T. Higashii, and H. Kitamura, "Evaluation of Amine-Based Solvent for Post-Combustion Capture of Carbon Dioxide", *Journal of Chemical Engineering of Japan* **47**, 663 (2014).

[5]K. Li, A. Cousins, H. Yu, P. Feron, M. Tade, W. Luo, and J. Chen, "Systematic Study of Aqueous Monoethanolamine-Based $CO_2$ capture Process: Model Development and Process Improvement", *Energy Science & Engineering* **4**, 23 (2016).

[6]A. Singh and K. Stéphenne, "Shell Cansolv Co2 Capture Technology: Achievement from First Commercial Plant", *Energy Procedia* **63**, 1678 (2014).

[7]Y. Liu, H.Z. Ye, K.M. Diederichsen, T. Van Voorhis, and T.A. Hatton, "Electrochemically Mediated Carbon Dioxide Separation with Quinone Chemistry in Salt-Concentrated Aqueous Media", *Nat Commun* **11**, 2278 (2020).

[8]M. Wang, H. Herzog, and T.A. Hatton, " $CO_2$ Capture Using Electrochemically Mediated Amine Regeneration", *Industrial & Engineering Chemistry Research* **59**, 7087 (2020).

[9]D.W. Keith, G. Holmes, D. St. Angelo, and K. Heidel, "A Process for Capturing $CO_2$ from the Atmosphere", *Joule* **2**, 1573 (2018).

[10]F.M. Brethomé, N.J. Williams, C.A. Seipp, M.K. Kidder, and R. Custelcean, "Direct Air Capture of Co2 Via Aqueous-Phase Absorption and Crystalline-Phase Release Using Concentrated Solar Power", *Nature Energy* **3**, 553 (2018).

[11]E.S. Sanz-Perez, C.R. Murdock, S.A. Didas, and C.W. Jones, "Direct Capture of $CO_2$ from Ambient Air", *Chem Rev* **116**, 11840 (2016).

[12]C.-F. de Lannoy, M.D. Eisaman, A. Jose, S.D. Karnitz, R.W. DeVaul, K. Hannun, and J.L.B. Rivest, "Indirect Ocean Capture of Atmospheric Co2: Part I. Prototype of a Negative Emissions Technology", *International Journal of Greenhouse Gas Control* **70**, 243 (2018).

[13]I.A. Digdaya, I. Sullivan, M. Lin, L. Han, W.H. Cheng, H.A. Atwater, and C. Xiang, "A Direct Coupled Electrochemical System for Capture and Conversion of $CO_2$ from Oceanwater", *Nat Commun* **11**, 4412 (2020).

[14]M. Lail, J. Tanthana, and L. Coleman, "Non-Aqueous Solvent (Nas) $CO_2$ Capture Process", *Energy Procedia* **63**, 580 (2014).

[15]D.J. Heldebrant, P.K. Koech, V.-A. Glezakou, R. Rousseau, D. Malhotra, and D.C. Cantu, "Water-Lean Solvents for Post-Combustion $CO_2$ Capture: Fundamentals, Uncertainties, Opportunities, and Outlook", *Chemical Reviews* **117**, 9594 (2017).
[16]R. Custelcean, N.J. Williams, X. Wang, K.A. Garrabrant, H.J. Martin, M.K. Kidder, A.S. Ivanov, and V.S. Bryantsev, "Dialing in Direct Air Capture of $CO_2$ by Crystal Engineering of Bisiminoguanidines", *ChemSusChem* **13**, 6381 (2020).
[17]M. Eisaman, D. Schwartz, S. Amic, D. Larner, J. Zesch, F. Torres, and K. Littau, "Energy-Efficient Electrochemical $CO_2$ Capture from the Atmosphere", presented at the Technical Proceedings of the 2009 Clean Technology Conference and Trade Show, 2009 (unpublished).
[18]S. Jin, M. Wu, R.G. Gordon, M.J. Aziz, and D.G. Kwabi, "Ph Swing Cycle for $CO_2$ Capture Electrochemically Driven through Proton-Coupled Electron Transfer", *Energy & Environmental Science* **13**, 3706 (2020).
[19]H. Xie, Y. Wu, T. Liu, F. Wang, B. Chen, and B. Liang, "Low-Energy-Consumption Electrochemical $CO_2$ Capture Driven by Biomimetic Phenazine Derivatives Redox Medium", *Applied Energy* **259**, (2020).
[20]H. Xie, W. Jiang, T. Liu, Y. Wu, Y. Wang, B. Chen, D. Niu, and B. Liang, "Low-Energy Electrochemical Carbon Dioxide Capture Based on a Biological Redox Proton Carrier", *Cell Reports Physical Science* **1**, (2020).
[21]R.E. Zeebe and D. Wolf-Gladrow, *$CO_2$ in Seawater: Equilibrium, Kinetics, Isotopes*. Elsevier Oceanography Series, ed. D. Halpern. Vol. **65**. (Elsevier, Amsterdam, 2005).
[22]Q. Chen, M.R. Gerhardt, and M.J. Aziz, "Dissection of the Voltage Losses of an Acidic Quinone Redox Flow Battery", *Journal of the Electrochemical Society* **164**, A1126 (2017).
[23]M.-A. Goulet and M.J. Aziz, "Flow Battery Molecular Reactant Stability Determined by Symmetric Cell Cycling Methods", *Journal of the Electrochemical Society* **165**, A1466 (2018).
[24]S.E. Renfrew, D.E. Starr, and P. Strasser, "Electrochemical Approaches toward $CO_2$ Capture and Concentration", *ACS Catalysis* **10**, 13058 (2020).
[25]J.S. Kang, S. Kim, and T.A. Hatton, "Redox-Responsive Sorbents and Mediators for Electrochemically Based $CO_2$ Capture", *Current Opinion in Green and Sustainable Chemistry* **31**, 100504 (2021).
[26]D. Broberg, C. Normile, and A.K. Stark, "Uncertainty Drives Carbon Ambition, Even as Deployment Potential Still at Some Remove", *Chem* **7**, 2854 (2021).
[27]S. Deutz and A. Bardow, "Life-Cycle Assessment of an Industrial Direct Air Capture Process Based on Temperature–Vacuum Swing Adsorption", *Nature Energy* **6**, 203 (2021).
[28]S. Fuss, W.F. Lamb, M.W. Callaghan, J. Hilaire, F. Creutzig, T. Amann, T. Beringer, W.d.O. Garcia, J. Hartmann, T. Khanna, G. Luderer, G.F. Nemet, J. Rogelj, P. Smith, J.L.V. Vicente, J. Wilcox, M.d.M.Z. Dominguez, and J.C. Minx, "Negative Emissions—Part 2: Costs, Potentials and Side Effects", *Environmental Research Letters* **13**, 063002 (2018).
[29]S. Voskian and T.A. Hatton, "Faradaic Electro-Swing Reactive Adsorption for $CO_2$ Capture", *Energy & Environmental Science* **12**, 3530 (2019).
[30]R. Sharifian, R.M. Wagterveld, I.A. Digdaya, C. Xiang, and D.A. Vermaas, "Electrochemical Carbon Dioxide Capture to Close the Carbon Cycle", *Energy & Environmental Science* (2021).

[31]Q. Shu, L. Legrand, P. Kuntke, M. Tedesco, and H. Hamelers, "Electrochemical Regeneration of Spent Alkaline Absorbent from Direct Air Capture", *Environmental Science & Technology* **54**, 8990 (2020).
[32]G.T. Rochelle, Y. Wu, E. Chen, K. Akinpelumi, K. Fischer, T. Gao, C. Liu, and J. Selinger, "Pilot Plant Demonstration of Piperazine with the Advanced Flash Stripper", *International Journal of Greenhouse Gas Control* **84**, 72 (2019).
[33]P.N.P.H. LLC, "W. A. Parish Post-Combustion Co2 Capture and Sequestration Project," 2017.
[34]S. Jin, Y. Jing, D.G. Kwabi, Y. Ji, L. Tong, D. De Porcellinis, M.A. Goulet, D.A. Pollack, R.G. Gordon, and M.J. Aziz, "A Water-Miscible Quinone Flow Battery with High Volumetric Capacity and Energy Density", *ACS Energy Letters* **4**, 1342 (2019).
[35]Y. Ji, M.A. Goulet, D.A. Pollack, D.G. Kwabi, S. Jin, D. Porcellinis, E.F. Kerr, R.G. Gordon, and M.J. Aziz, "A Phosphonate-Functionalized Quinone Redox Flow Battery at near-Neutral Ph with Record Capacity Retention Rate", *Advanced Energy Materials* **9**, 1900039 (2019).
[36]E.S. Beh, D. De Porcellinis, R.L. Gracia, K.T. Xia, R.G. Gordon, and M.J. Aziz, "A Neutral Ph Aqueous Organic-Organometallic Redox Flow Battery with Extremely High Capacity Retention", *ACS Energy Letters* **2**, 639 (2017).
[37]S. Jin, E.M. Fell, L. Vina-Lopez, Y. Jing, P.W. Michalak, R.G. Gordon, and M.J. Aziz, "Near Neutral pH Redox Flow Battery with Low Permeability and Long-Lifetime Phosphonated Viologen Active Species", *Advanced Energy Materials* **10**, 2000100 (2020).
[38]D.G. Kwabi, K. Lin, Y. Ji, E.F. Kerr, M.-A. Goulet, D. De Porcellinis, D.P. Tabor, D.A. Pollack, A. Aspuru-Guzik, R.G. Gordon, and M.J. Aziz, "Alkaline Quinone Flow Battery with Long Lifetime at pH 12", *Joule* **2**, 1907 (2018).
[39]B. Hu, C. DeBruler, Z. Rhodes, and T.L. Liu, "Long-Cycling Aqueous Organic Redox Flow Battery (Aorfb) toward Sustainable and Safe Energy Storage", *J Am Chem Soc* **139**, 1207 (2017).
[40]C.L. Huang, C.J. Liu, K.J. Wu, H.R. Yue, S.Y. Tang, H.F. Lu, and B. Liang, " $CO_2$ Capture from Flue Gas Using an Electrochemically Reversible Hydroquinone/Quinone Solution", *Energy & Fuels* **33**, 3380 (2019).
[41]M. Ulaganathan, V. Aravindan, Q. Yan, S. Madhavi, M. Skyllas-Kazacos, and T.M. Lim, "Recent Advancements in All-Vanadium Redox Flow Batteries", *Advanced Materials Interfaces* **3**, 1500309 (2016).

**Electronic Supplementary Information**

*for*

# Low Energy Carbon Capture via Electrochemically Induced pH Swing with Electrochemical Rebalancing

Shijian Jin[†], Min Wu[†], Yan Jing[‡], Roy Gordon[‡] and Michael J. Aziz[†*]

[†] John A. Paulson School of Engineering and Applied Sciences, Harvard University, Cambridge, Massachusetts, 02138, United States

[‡]Department of Chemistry and Chemical Biology, Harvard University, Cambridge, Massachusetts 02138, United States

*maziz [at] harvard [dot] edu

## Table of Sections



## Table of Additional Figures

**Table S 1| Table of acronyms**

| Acronyms | Explanation |
|---|---|
| BPMED | bipolar membrane electrodialysis |
| CEM | cation exchange membrane |
| DAC | direct air capture |
| DIC | dissolved inorganic carbon |
| $DIC_x$ | concentration of dissolved inorganic carbon in state "x" |
| $\Delta DIC_{flow,x\rightarrow y}$ | change in DIC between states "x" and "y" ($DIC_y - DIC_x$), measured by flow meter and $CO_2$ sensor |
| $\Delta DIC_{TA-pH,x\rightarrow y}$ | change in DIC between states "x" and "y" ($DIC_y - DIC_x$), measured by known total alkalinity and measured pH |
| $\Delta DIC_{TA-eq,x\rightarrow y}$ | change in DIC between states "x" and "y" ($DIC_y - DIC_x$), measured by by known total alkalinity and assuming gas-solution equilibrium |
| DOC | direct ocean capture |
| DSPZ | sodium 3,3'-(phenazine-2,3-diylbis(oxy))bis(propane-1-sulfonate) |
| $DSPZH_2$ | reduced DSPZ |
| EMAR | electrochemically mediated amine regeneration |
| $K_3Fe(CN)_6$ | potassium ferricyanide (oxidized form of $Fe(CN)_6$) |
| $K_4Fe(CN)_6$ | potassium ferrocyanide (reduced form of $Fe(CN)_6$) |
| MFC | mass flow controller |
| $p_1$ | $CO_2$ partial pressure in bar during $CO_2$ capture (inlet) |
| $p_3$ | $CO_2$ partial pressure in bar during $CO_2$ outgassing (exit) |
| PCET | proton-coupled electron transfer |
| $pH_{mea}$ | pH measured by pH probe |
| $pH_{TA-eq}$ | pH calculated using known total alkalinity and assuming gas-solution equilibrium |
| TA | total alkalinity |
| $TA_x$ | concentration of total alkalinity in state "x" |
| $\Delta TA_{x\rightarrow y}$ | change in TA between states "x" and "y" ($TA_y - TA_x$), measured by counting charges during deacidification or acidification, which is equivalent to twice the concentration of DSPZ. |

## 1 $CO_2$ Molar Ideal Cycle Work

For a system with given $TA_{3'i}$ and $\Delta TA_{3\to1}$, i.e. DSPZ concentration, the ideal cycle work is defined as the work input for driving the system through electrochemical deacidification at $p_1$ and a subsequent electrochemical acidification at $p_3$, at an infinitesimal current. In the ideal cycle, gas-solution equilibrium is assumed at every point and because TA is known, $pH_{TA-eq}$ and $DIC_{TA-eq}$ at every point can be calculated. The $CO_2$ molar ideal cycle work, which we denote as $\bar{w}_{ideal}$, is obtained from dividing the ideal cycle work by expected $\Delta DIC_{3\to1}$, i.e. $\Delta DIC_{TA-eq,3\to1}$.

This section explains how $\bar{w}_{ideal}$ is calculated in detail. Both of the ideal cycle work and $\Delta DIC_{TA-eq,3\to1}$ are governed by these parameters: initial TA ($TA_{3'i}$ or simply $TA_{3'}$ because $TA_{3'i}$ and $TA_{3'f}$ will be the same in an ideal cycle), $\Delta TA_{3\to1}$ and $pCO_2$ at $p_1$, and the following equations:

$$\mathrm{DIC} = [\mathrm{CO_2(aq)}] + [\mathrm{HCO_3^-}] + [\mathrm{CO_3^{2-}}]; \tag{1}$$

$$\mathrm{K_1} = \frac{[\mathrm{HCO_3^-}][\mathrm{H^+}]}{[\mathrm{CO_2(aq)}]}; \tag{2}$$

$$\mathrm{K_2} = \frac{[\mathrm{CO_3^{2-}}][\mathrm{H^+}]}{[\mathrm{HCO_3^-}]}; \tag{3}$$

$$\mathrm{TA} \equiv [\mathrm{OH^-}] + [\mathrm{HCO_3^-}] + 2[\mathrm{CO_3^{2-}}] - [\mathrm{H^+}]; \tag{4}$$

$$[\mathrm{S^+}] - [\mathrm{S^-}] = \mathrm{TA}; \tag{5}$$

$$[\mathrm{H^+}][\mathrm{OH^-}] = 10^{-14}, \tag{6}$$

where the $K_1$ and $K_2$ used here are $1.1 \times 10^{-6}$ M and $4.1 \times 10^{-10}$ M,[1] resulting in the first and second $p$Ka for carbonic acid being 6.0 and 9.4, respectively. Eq. S4 is the definition of TA of the solution under consideration and eq. S5 arises from the charge neutrality constraint in solution ($S^+$ and $S^-$ correspond to the cationic and anionic species of the electrolyte salt). During deacidification, $[S^+]$ increases in the negolyte reservoir, so TA increases as well (eq. S5), which means an increase of hydroxide concentration or $[HCO_3^-]$ or $[CO_3^{2-}]$ given nonzero $pCO_2$ (eq. S4). The reverse happens during acidification. The expressions for the concentration of each constituent of DIC can be derived by rearranging the above equations:

$$[\mathrm{CO_2(aq)}] = \frac{\mathrm{DIC}}{1 + \frac{\mathrm{K_1}}{[\mathrm{H^+}]} + \frac{\mathrm{K_1K_2}}{[\mathrm{H^+}]^2}}; \tag{7}$$

$$[\mathrm{HCO_3^-}] = \frac{\mathrm{DIC}}{1 + \frac{[\mathrm{H^+}]}{\mathrm{K_1}} + \frac{\mathrm{K_2}}{[\mathrm{H^+}]}}; \tag{8}$$

$$[CO_3^{2-}] = \frac{DIC}{1 + \frac{[H^+]}{K_2} + \frac{[H^+]^2}{K_1 K_2}}; \quad (9)$$

$TA_{3'}$ is calculated using eq. S7, measured pH and assumed gas-solution equilibrium, i.e.

$$[CO_2(aq)] = 0.035 \times pCO_2. \quad (10)$$

where 0.035 comes from Henry's Law constant of 35 mM bar$^{-1}$ at room temperature and the units of $[CO_2(aq)]$ and $pCO_2$ are Molar and bars, respectively. For example, in **Table 1**, $pH_{meas}$ at state $3'_i$ was 7.4, and $pCO_2$ was 0.1 bar, so DIC can be derived from eq. S7 and S10, and subsequently $[HCO_3^-]$ and $[CO_3^{2-}]$ from eq. S8 and S9, respectively. $TA_{3'i}$ is then obvious from eq. S4. Because $\Delta TA_{3'i\rightarrow1}$, which is determined by the concentration of DSPZ, is equal to $\Delta TA_{3\rightarrow1}$, and $-\Delta TA_{1'\rightarrow3}$ (or $-\Delta TA_{1\rightarrow3}$) in the ideal cycle, TA at states 1, 1' and 3 can be derived from $TA_{3'i}$ and $\Delta TA$ values. Because TA and $pCO_2$ is known for each state, $pH_{TA-eq}$ and $DIC_{TA-eq}$ can be calculated. Then $\Delta DIC_{TA-eq,3\rightarrow1}$ is simply $DIC_{TA-eq,1}$ minus $DIC_{TA-eq,3}$. In fact, we can calculate TA, $pH_{TA-eq}$ and $DIC_{TA-eq}$ of every point in between the states as well, and hence construct the ideal cycles. Because of the $2H^+/2e^-$ redox processes of DSPZ,[2] its reduction potential, and overall cell potential decreases 59 mV for every unit of increase in pH. This allows us to calculate the ideal cycle work using the following equation:

$$w_{cycle,ideal} = \sum_{n=1} 0.059 \times (pH_{deacidification}(TA(n)) - pH_{acidification}(TA(n)) \times \Delta TA \times F \quad (11)$$

Where *n* is the index, *TA* increases by $\Delta TA$ Molar when n increases by 1, pH is a function of *TA* and the process, 0.059 (V/pH) is the conversion factor between pH and cell voltage, *F* is the Faraday constant (96485 C mole$^{-1}$) and the unit of $w_{cycle,ideal}$ is J L$^{-1}$. Then $\bar{w}_{ideal}$ follows naturally by dividing $w_{cycle,ideal}$ by $\Delta DIC_{3\rightarrow1}$.

$$\bar{w}_{ideal} = \frac{w_{cycle,ideal}}{\Delta DIC_{TA-eq,3\rightarrow1}} \quad (12)$$

As mentioned in the main text, $\Delta DIC$ values vary as $p_1$, $TA_{3'}$ and $\Delta TA_{3\rightarrow1}$ change. **Fig. 4 e, f** and **g** show the ideal cycles for various $p_1$ given fixed $p_3$, $TA_{3'}$ and $\Delta TA_{3\rightarrow1}$. The amount of $CO_2$ captured in process $3'i\rightarrow1$ and monitored by the flow meter and the $CO_2$ sensor is around 50 mL, which translates to 0.21 M $\Delta DIC_{flow,3'i\rightarrow1}$, assuming $T$ = 293 K and $p$ = 1 bar, across all different $p_1$ values (**Fig. 4a**). This similarity is consistent with the ideal cycle behavior, illustrated in **Fig. 4 c** and the alignment of measured $\Delta DIC_{flow,3'i\rightarrow1}$ with the theoretical $\Delta DIC_{TA-eq,3'\rightarrow1}$ *vs.* $pCO_2$ curve. The similar amount of $CO_2$ captured and released, i.e. $\Delta DIC_{flow,3'i\rightarrow1}$ and $\Delta DIC_{flow,1'\rightarrow3}$, is caused by the coincidental resemblance of the slopes of the two-stage deacidification+$CO_2$ invasion and the two-stage acidification+$CO_2$ outgassing processes under the experimental conditions (**Fig. 4 c**). The agreement of $\Delta DIC_{TA-eq,3'\rightarrow1}$ *vs.* $pCO_2$ and $\Delta DIC_{TA-eq,1'\rightarrow3}$ *vs.* $pCO_2$ curves at high $p_1$ values also corroborates the flow measurements. If the $p_1$ were 0.4 mbar instead, the deacidification and acidification processes would have significantly different slopes so the amounts of $CO_2$ captured during deacidification and released during acidification would be different, as shown in **Fig. S 1 e**.

Here we plot the ideal cycles for varying $TA_{3'}$ and fixed $p_1 = 0.4$ mbar, $p_3 = 1$ bar and $\Delta TA_{3\rightarrow1} = 0.21$ M (**Fig. S 1)**. The plots illustrate the effect of varying $TA_{3'}$ on $w_{cycle,ideal}$, $\Delta DIC_{TA-eq}$, and $\overline{w}_{ideal}$.

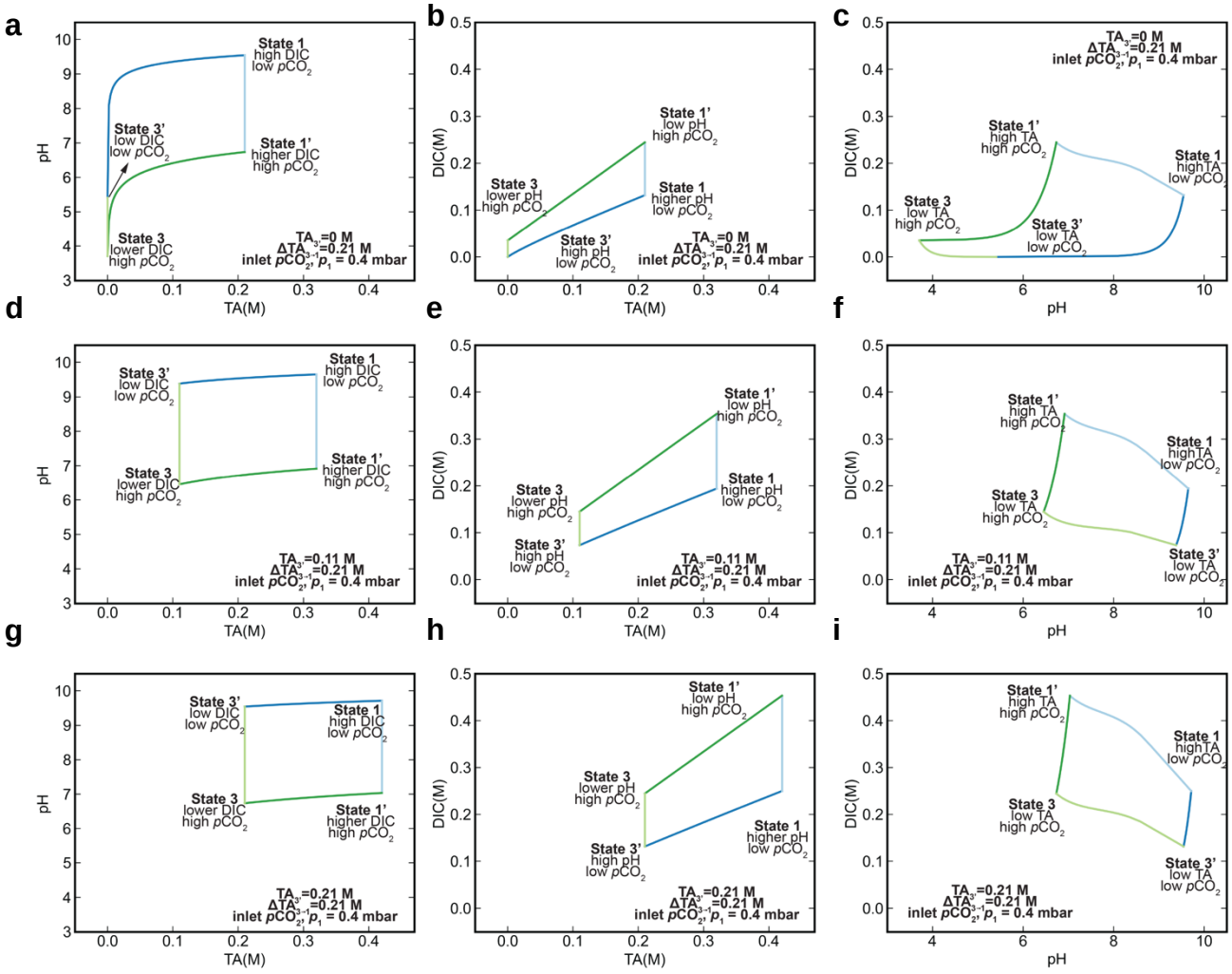


**Fig. S 1| Ideal cycles constructed using $p_1 = 0.4$ mbar and $p_3 = 1$ bar, $\Delta TA_{3\rightarrow1} = 0.21$ M and varying $TA_{3'}$. a-c**, $TA_{3'} = 0.0$ M; **d-f**, $TA_{3'} = 0.11$ M and **g-i**, $TA_{3'} = 0.21$ M;

The area enclosed by the cycles in **Fig. S 1a, d** and **g**, is proportional to the ideal cycle work for the cycles with fixed $p_1 = 0.4$ mbar, $p_3 = 1$ bar, $\Delta TA_{3\rightarrow1} = 0.21$ M and $TA_{3'}$ being 0.0, 0.11 and 0.21 M, respectively. The area roughly stays the same as $TA_{3'}$ increases, but $\Delta DIC_{TA-eq,3\rightarrow1}$ shrinks significantly, as shown in **Fig. S 1b, e** and **h**. As a result, $\overline{w}_{ideal}$ increases as $TA_{3'}$ increases. With $TA_{3'}$ being 0.0, 0.11 and 0.21 M, the ideal cycle work is 3.58, 3.40 and 3.31 kJ $L^{-1}$, respectively, $\Delta DIC_{TA-eq,3\rightarrow1}$ is 0.097, 0.049 and 0.005 M, respectively and the resulting $\overline{w}_{ideal}$ is 37.02, 69.31 and 661.9 kJ $mol_{CO2}^{-1}$, respectively.

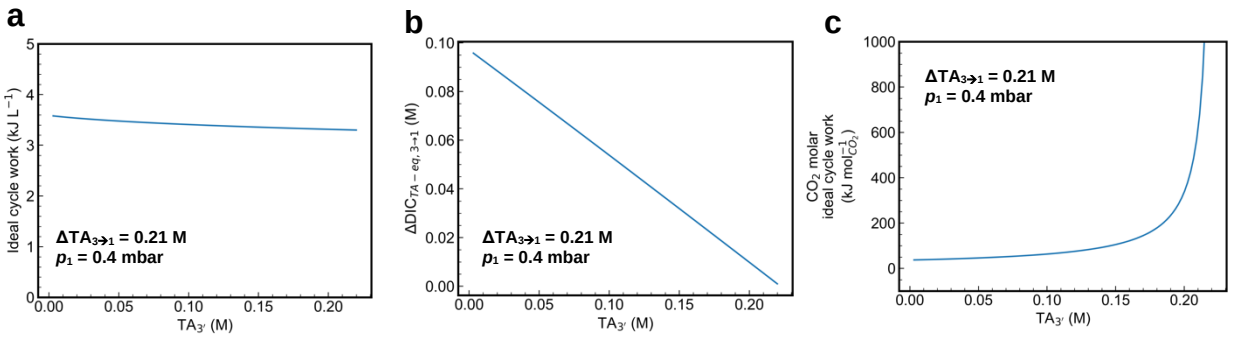


**Fig. S 2| Dependence of (a) $w_{cycle,ideal}$, (b) $\Delta DIC_{TA-pH,3\rightarrow1}$ (c) and $\overline{w}_{ideal}$ on $TA_{3'}$ in the ideal cycles with $p_1$ = 0.4 mbar, and $p_3$ = 1 bar, $\Delta TA_{3\rightarrow1}$= 0.21 M.**

**Fig. S 2** shows the dependence of $w_{cycle,ideal}$, $\Delta DIC_{TA-eq,3\rightarrow1}$ and $\overline{w}_{ideal}$ on $TA_{3'}$. Again, $\overline{w}_{ideal}$ increases with increasing $TA_{3'}$ because of the linearly decreasing $\Delta DIC_{TA-pH,3\rightarrow1}$ in the denominator of eq. S11.

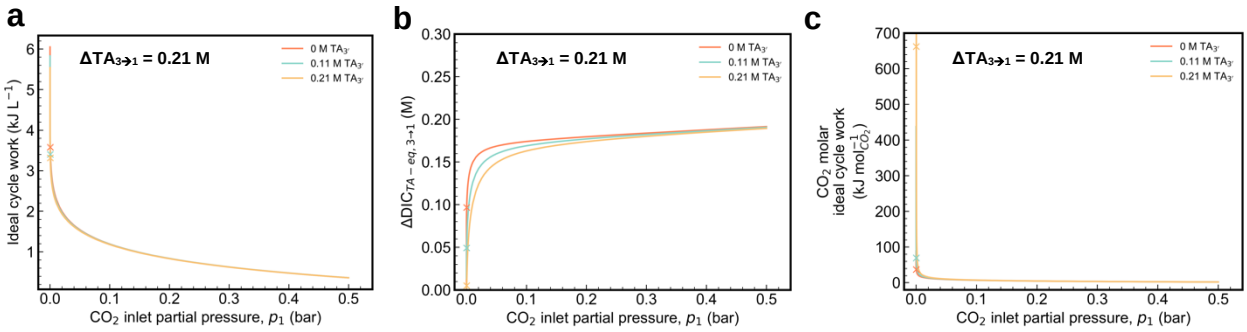


**Fig. S 3| Dependence of (a) $w_{cycle,ideal}$, (b) $\Delta DIC_{TA-eq,3\rightarrow1}$ and (c) $\overline{w}_{ideal}$ on $p_1$ in the ideal cycles with $\Delta TA_{3\rightarrow1}$ = 0.21 M and $TA_{3'}$ = 0.0, 0.11 and 0.21 M. The 'x' marks indicate $p_1$ = 0.4 mbar.**

**Fig. S 3** shows the dependence of $w_{cycle,ideal}$, $\Delta DIC_{TA-eq,3\rightarrow1}$ and $\overline{w}_{ideal}$ on $p_1$. $w_{cycle,ideal}$ decreases as $p_1$ increases because of lower negolyte pH, hence cell potential, during deacidification, but the curves are almost identical for different $TA_{3'}$ values. The $\Delta DIC_{TA-eq,3\rightarrow1}$ vs. $p_1$ curves for different $TA_{3'}$ are similar for large $pCO_2$ values, but significantly different at low $p_1$. Therefore, to keep $\overline{w}_{ideal}$ low for any inlet pressure $p_1$, high $TA_{3'}$ should be avoided.

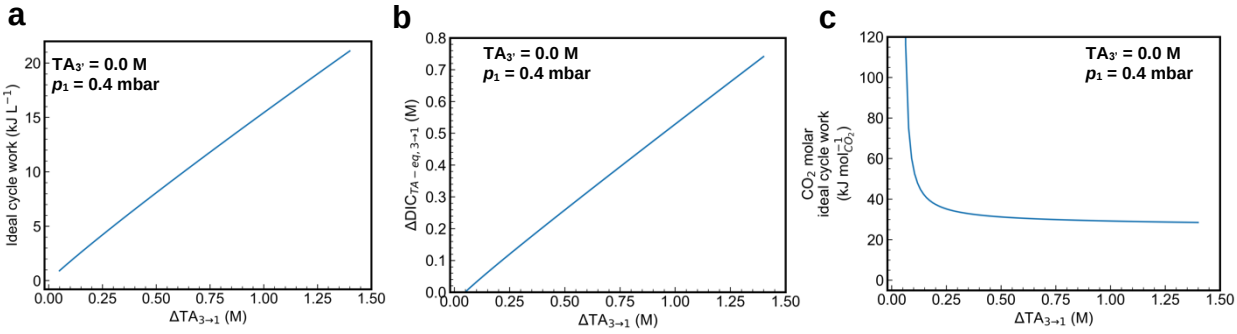


**Fig. S 4| Dependence of (a) $w_{cycle,ideal}$, (b) $\Delta DIC_{TA-eq,3\rightarrow1}$ and (c) and $\overline{w}_{ideal}$ on $\Delta TA_{3\rightarrow1}$ in the ideal cycles with $p_1$ = 0.4 mbar, $p_3$ = 1 bar and $TA_{3'}$ = 0.0 M.**

The last parameter that affects $w_{cycle,ideal}$, $\Delta DIC_{TA-eq,3\rightarrow1}$ and $\overline{w}_{ideal}$ is $\Delta TA_{3\rightarrow1}$, which is equivalent to twice the amount of DSPZ concentration. DSPZ has a solubility of 0.7 M in 1 M KCl or 1 M

KOH aqueous solution, so the largest $\Delta TA_{3\rightarrow1}$ it can induce is 1.4 M. **Fig. S 4** shows the dependence of $w_{cycle,ideal}$, $\Delta DIC_{TA-eq,3\rightarrow1}$ and $\overline{w}_{ideal}$ on $\Delta TA_{3\rightarrow1}$ for cycles with $TA_{3'}$ = 0.0 M, $p_1$ = 0.4 mbar and $p_3$ = 1 bar. Not surprisingly, $w_{cycle,ideal}$ and $\Delta DIC_{TA-eq,3\rightarrow1}$ increase with $\Delta TA_{3\rightarrow1}$ but the difference in their increase rate causes $\overline{w}_{ideal}$ to decrease with larger $\Delta TA_{3\rightarrow1}$. At 1.4 M $\Delta TA_{3\rightarrow1}$, $\overline{w}_{ideal}$ is 28.45 kJ $mol_{CO2}^{-1}$, which is 23% lower than 37.02 kJ $mol_{CO2}^{-1}$ for 0.21 M $\Delta TA_{3\rightarrow1}$. Assuming that similar second law efficiency holds for experimental cycles with different $\Delta TA_{3\rightarrow1}$ and same $p_1$, $p_3$ and $TA_{3'}$, using higher concentration of DSPZ can further decrease the cycle work for $CO_2$ separation from 108.1 kJ $mol_{CO2}^{-1}$to 99.5 kJ $mol_{CO2}^{-1}$. With the same reasoning, if a PCET molecule that undergoes 2-$e^-$ transfer and has 10 M solubility is developed, the ideal cycle work could be as low as 24 kJ $mol_{CO2}^{-1}$, leading to an actual cycle work of 95 kJ $mol_{CO2}^{-1}$.

## 2 Cycle Data

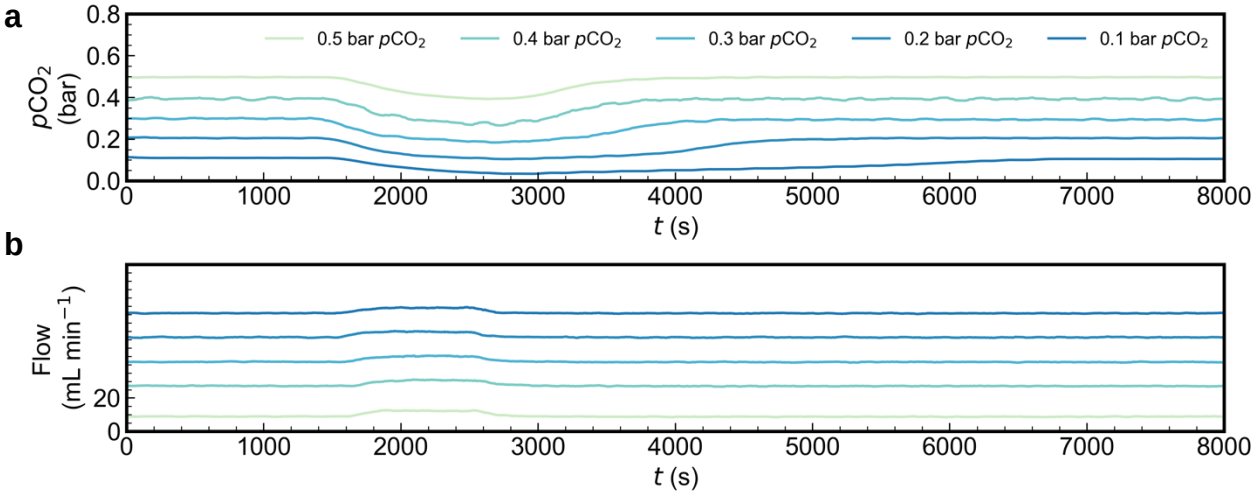


**Fig. S 5| Duration of the $CO_2$ capture and release processes in the cycles with 40 mA cm$^{-2}$ current density. a,** Downstream $pCO_2$ of one capture half cycle for each of the inlet $pCO_2$ conditions. **b,** Filtered total gas flow rate of one outgassing half cycle for each of the inlet $pCO_2$ conditions. All the processes look identical because of the same exit condition, so an arbitrary offset is added to differentiate the curves.

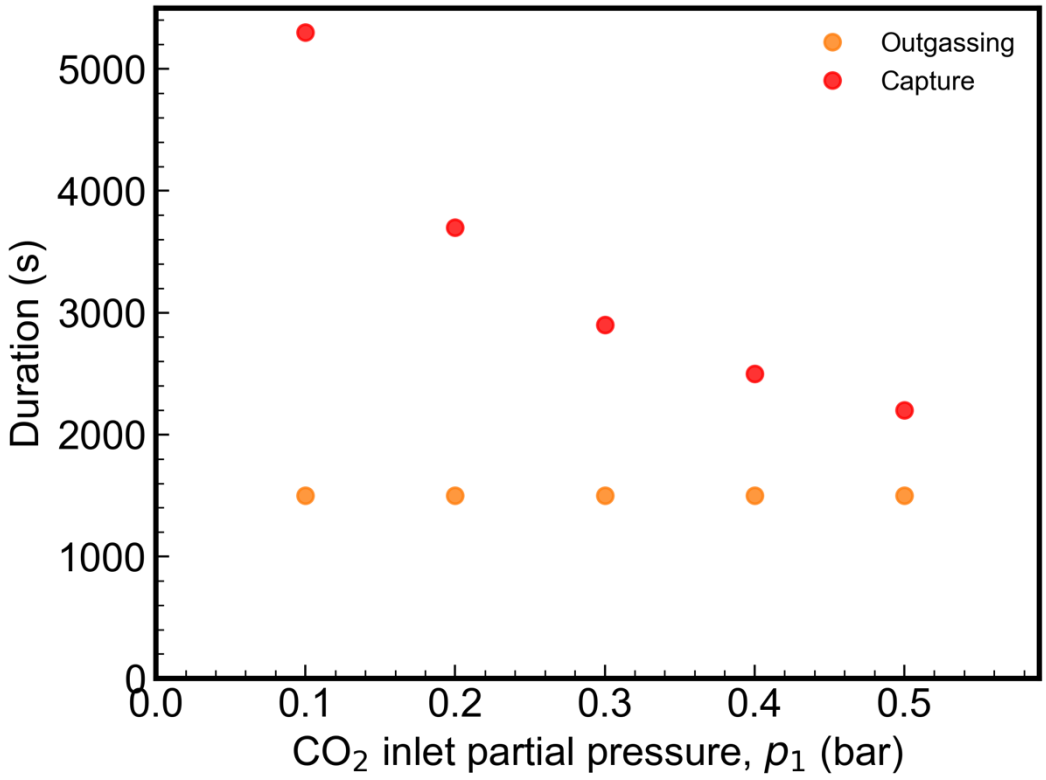


**Fig. S 6| Capture and outgassing durations extracted from Fig. S 5 a and b.**

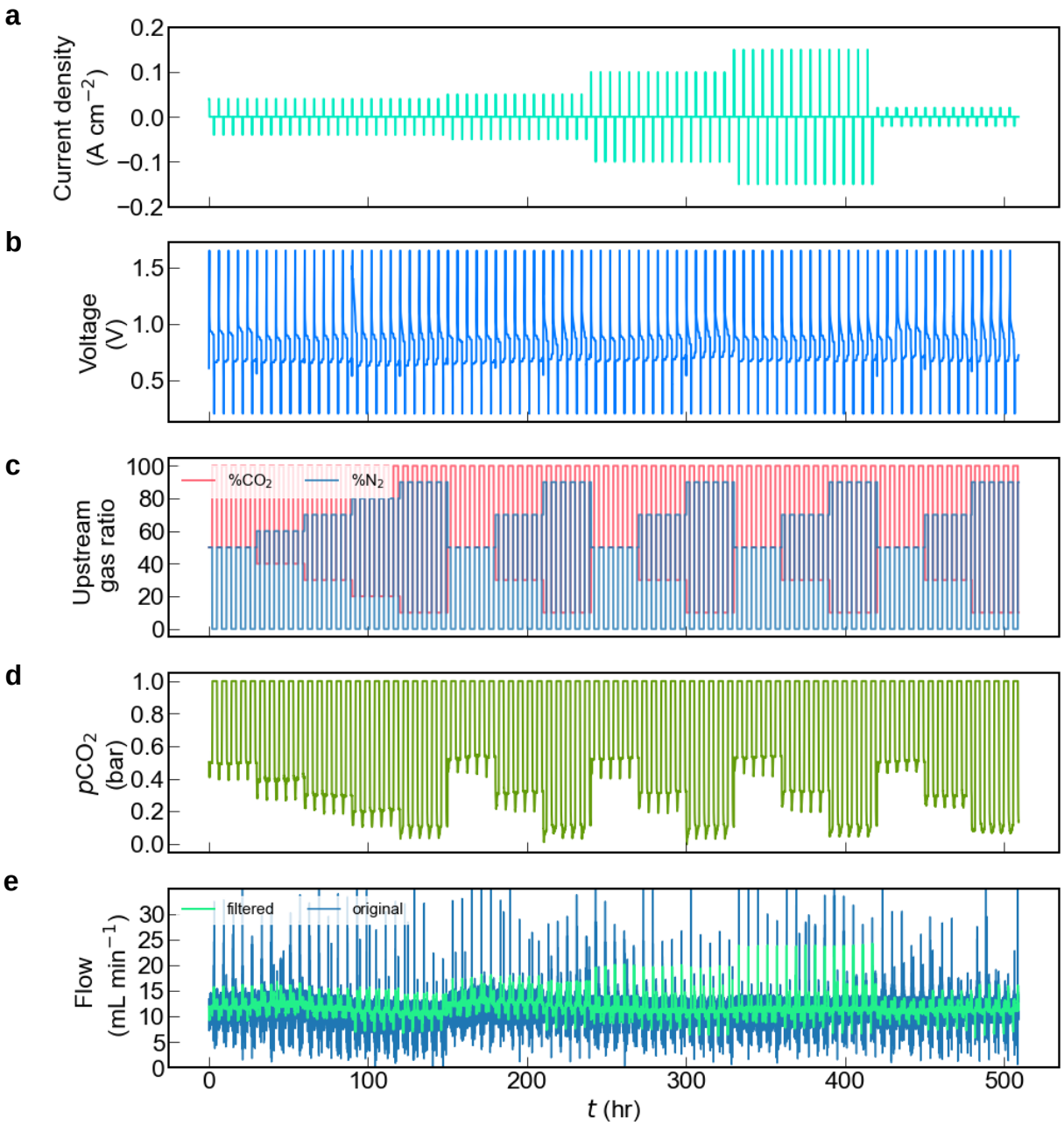


**Fig. S 7| Eighty-five $CO_2$ concentrating cycles with varying inlet *p*$CO_2$ and current densities.** These are the raw data for Fig. 5. Same cell was used as in **Fig 2**. Liquid pumping rate is 50 mL $min^{-1}$ for all the cycles. Note that, the pH measurements for high current densities are inaccurate, as the pH should never be able to reach pH > 14 for 0.11 M DSPZ. **a**, Current density. **b**, Voltage. **c**, $N_2$ and $CO_2$ percentage in the upstream source gas, controlled by mass flow controllers. **d**, $CO_2$ partial pressure. **e**, Total gas flow rate.

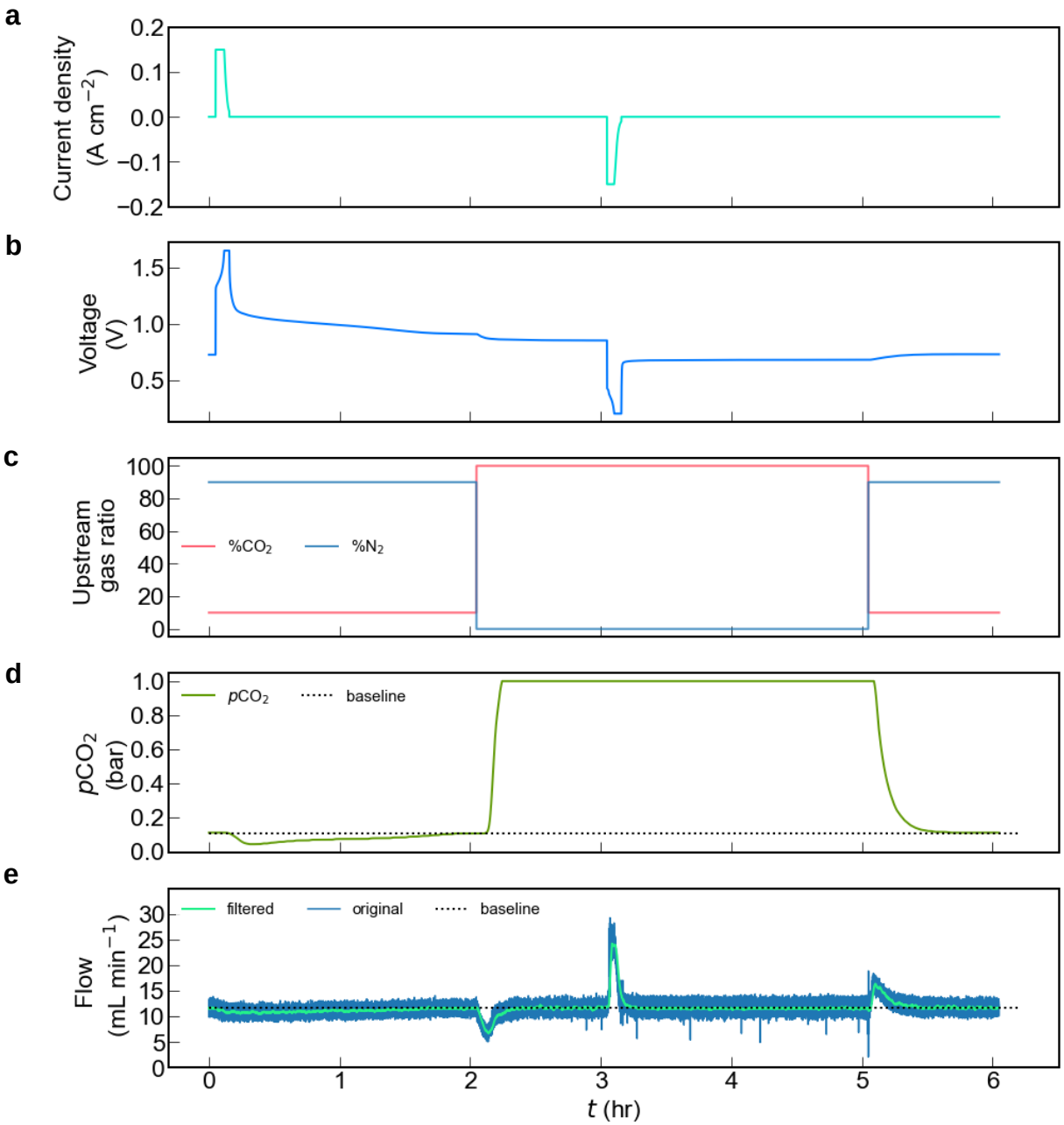


**Fig. S 8| One $CO_2$ concentrating cycle from Fig. S 7 with 0.1 bar inlet $pCO_2$ and 1 bar exit $pCO_2$ at 150 mA cm$^{-2}$.** Note that, the pH measurements are not shown because of an inexplicable artifact only present at high current, so it is invalid to extract $DIC_{TA-pH}$ for this condition. However, $DIC_{TA-eq}$ can be extracted because sufficient gas-solution is reached, as demonstrated by fact that the *p*CO2 and flow curves return to their baselines after $CO_2$ invasion and outgassing. **a**, Voltage profile. **b**, Current density. **c**, $N_2$ and $CO_2$ percentage in the upstream source gas, controlled by MFC. **d**, $CO_2$ partial pressure. **e**, Total gas flow rate.

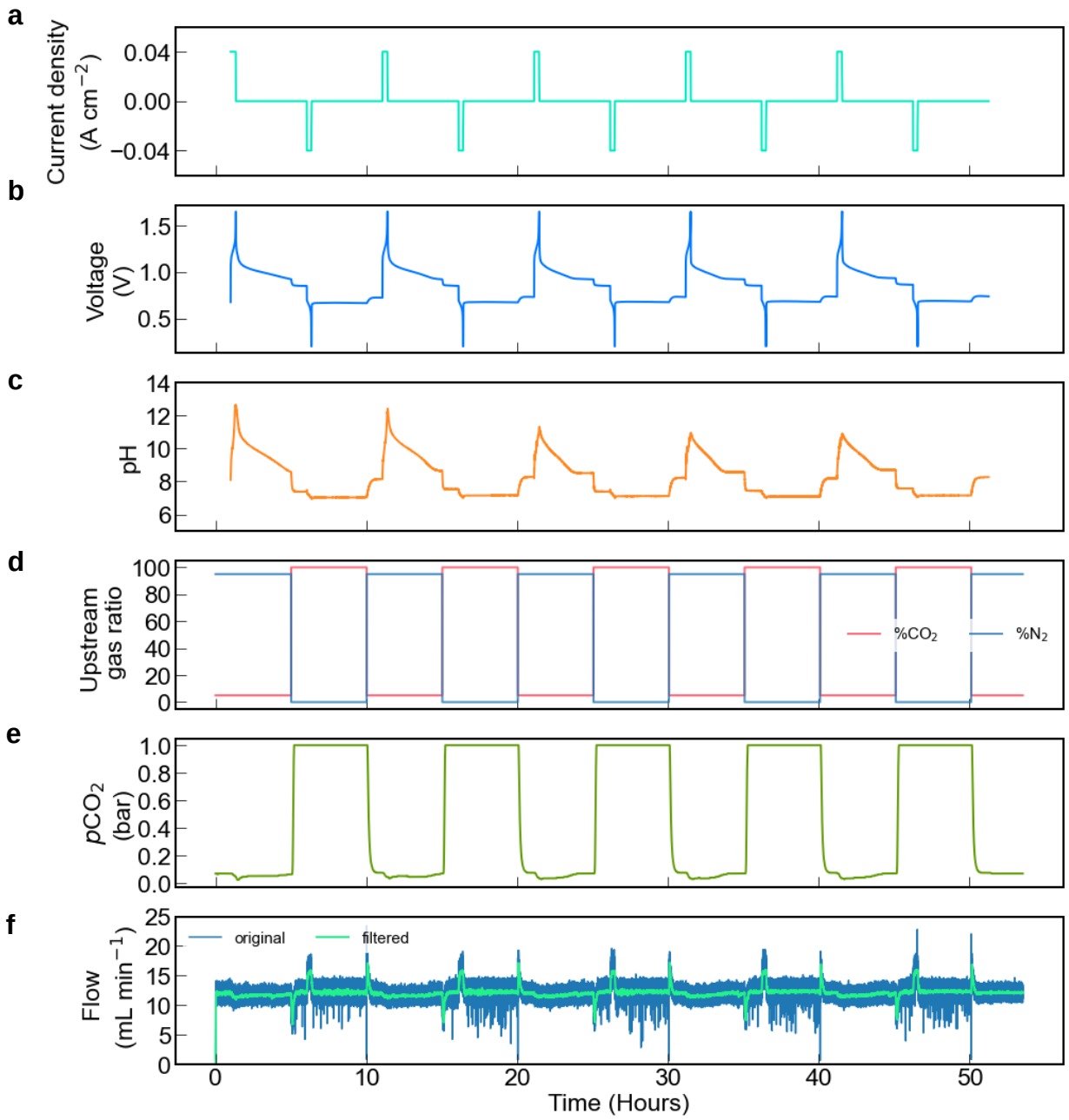


**Fig. S 9| Five $CO_2$ concentrating cycles with 0.05 bar inlet $pCO_2$ and 1 bar exit $pCO_2$ at 40 mA cm$^{-2}$.** Same cell was used as in **Fig. 2**. Fresh negolyte and posolyte were used. The liquid pumping rate is 150 mL min$^{-1}$, which is 50% faster than for capture at higher inlet pressure. **a**, Voltage profile. **b**, Current density. **c**, pH of the negolyte. **d**, $N_2$ and $CO_2$ percentage in the upstream source gas, controlled by mass flow controllers. **e**, $CO_2$ partial pressure. **f**, Total gas flow rate.

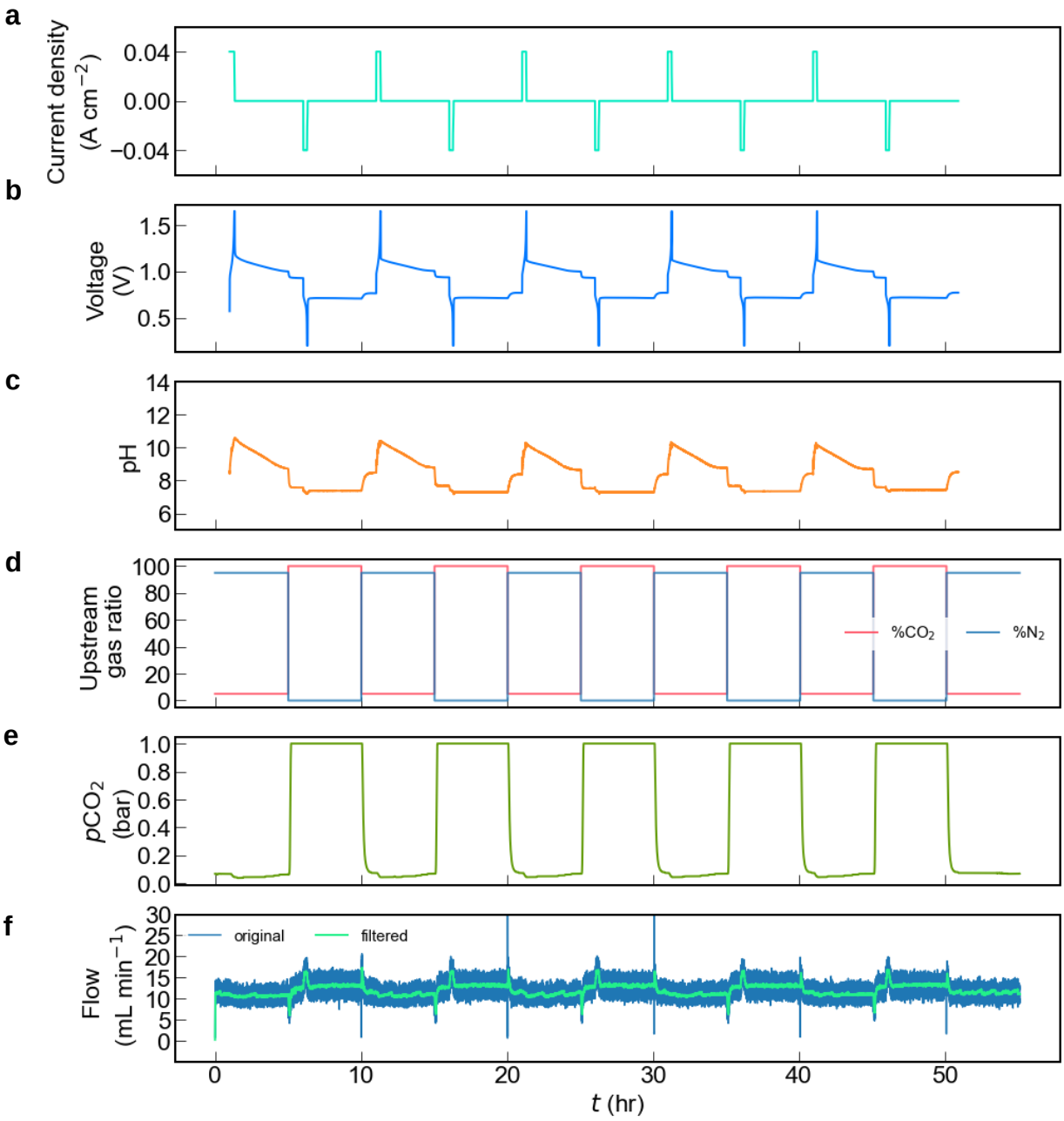


**Fig. S 10| Post-electrochemical rebalancing $CO_2$ capture with 0.05 bar inlet $pCO_2$ and 1 bar exit $pCO_2$ at 40 mA cm$^{-2}$.** Same cell was used as in **Fig.2**. Same posolyte and negolyte as in **Fig. S 9** were used. The liquid pumping rate is 150 mL min$^{-1}$. **a**, Voltage profile. **b**, Current density. **c**, pH of the negolyte. **d**, $N_2$ and $CO_2$ percentage in the upstream source gas, controlled by mass flow controllers. **e**, $CO_2$ partial pressure. **f**, Total gas flow rate. The system has the same carbon capture/release capability after the post-electrochemical rebalancing.

## 3 More on Electrochemical Rebalancing

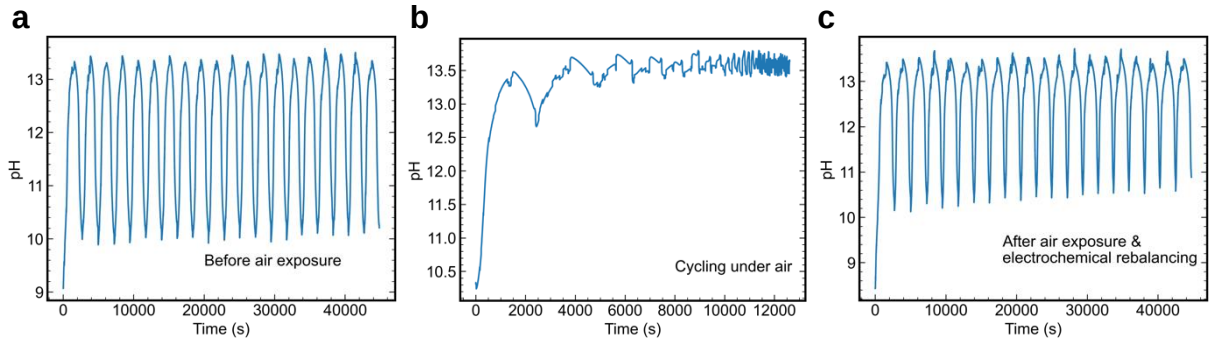


**Fig. S 11| pH of the negolyte during cycles before air exposure (a), under air (b) and after electrochemical rebalancing (c), respectively.** pH drifts up because of oxygen presence.

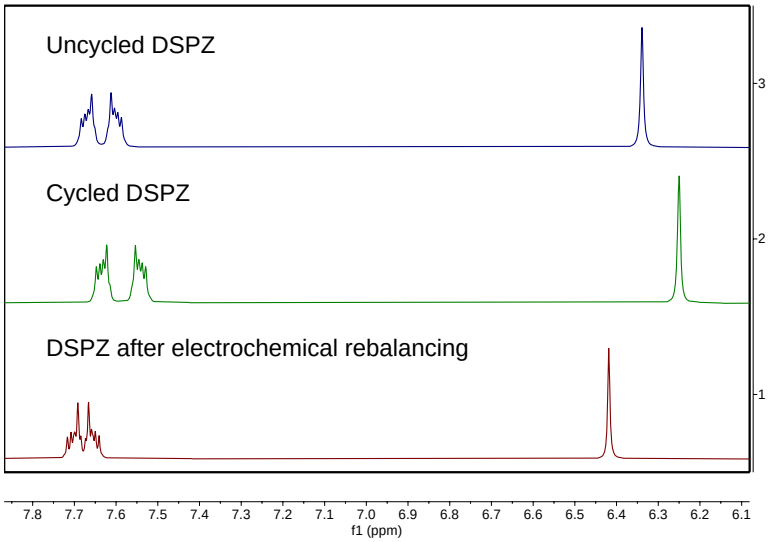


**Fig. S 12| NMR spectra of aromatic region of (top) uncycled DSPZ, (middle) DSPZ after cycling under air, and (bottom) DSPZ after electrochemical rebalancing.** No new peaks in the aromatic region were observed. The slight peak shifts were caused by concentration and pH differences.

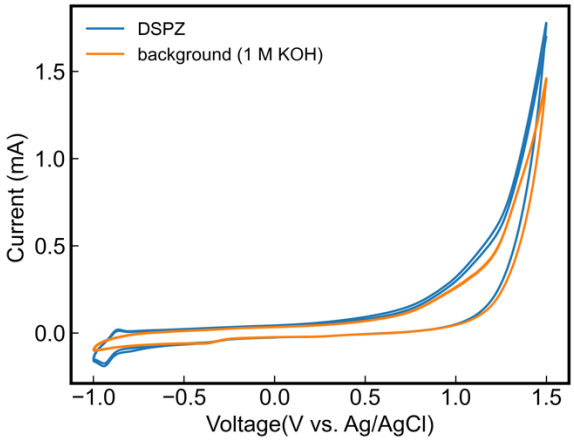


**Fig. S 13| Cyclic voltammetry of DSPZ and 1 M KOH background.** No additional peak was observed for DSPZ during the oxidative scan, indicating absence of side reactions.

**Fig. 1b** lists all the reactions related to carbon capture in our system. When all reactions involving $CO_2$ are removed, the system is the same as an aqueous organic redox flow battery (AORFB).[3-5] The electrochemical rebalancing method is also applicable to AORFB when there is an oxygen leakage. **Fig. 6** demonstrates the application of the electrochemical rebalancing method in an AORFB and carbon capture flow cell, which both are organic PCET systems that have pH swing ranging from neutral to basic. **Fig. S 12** shows that there are no new peaks generated in the aromatic region in the NMR spectra, indicating the absence of side reactions during electrochemical rebalancing. Here we suggest that the electrochemical rebalancing method also applies to other aqueous based electrochemical systems, including organic and inorganic, PCET or non-PCET, acidic or basic, dissolved or solid redox active materials. If no side reaction is triggered by the oxidative voltage, which is the case for DSPZ as shown in **Fig. S 13**, the electrochemical rebalancing method can be applied. Here are several examples.

*Organic Non-PCET system in neutral aqueous solution: $Fe(CN)_6$ (posolyte) | Viologen (negolyte) Flow Battery*

When the viologen-based redox flow battery[6-8] is charged: oxygen can chemically oxidize the reduced viologen to the oxidized state, accumulating hydroxide in the negolyte, leading to the negolyte to discharged state and the posolyte active species maintaining the oxidized state. Because the redox active core of viologens have two positive charges, we denote their oxidized form as $Vi^{2+}$ and the single-electron reduced form as $Vi^{+}$. The negolyte side is discharged when oxygen is present, i.e. :

$$\frac{1}{2}O_2 + 2\,Vi^{+} + H_2O \rightarrow 2\,Vi^{2+} + 2\,OH^{-}$$

The electrochemical rebalancing method can remove the accumulated hydroxide, repelling $O_2$ in the negolyte reservoir:

$$2\,OH^{-} \rightarrow \frac{1}{2}O_2 + H_2O + 2\,e^{-}$$

During the electrochemical rebalancing process, the electrons are transferred to the posolyte side, which has accumulated $Fe(CN)_6^{3-}$ , and eventually both negolyte and posolyte sides are recover the their initial composition, i.e. $Fe(CN)_6^{4-}$ in posolyte and $Vi^{2+}$ in negolyte, rebalancing the system.

*Inorganic Non-PCET system in strongly acidic aqueous solution: $VO^{2+}/VO_2^{+}$ (posolyte) | $V^{3+}/V^{2+}$ (negolyte) Flow Battery*

When a vanadium redox flow battery[9] negolyte contains the charged form, i.e. $V^{2+}$: if oxygen diffuses into the negolyte, it can chemically oxidize $V^{2+}$ to $V^{3+}$, and hydroxide is accumulated in the negolyte,

$$\frac{1}{2}\,O^2 + 2\,V^{2+} + H_2O \rightarrow 2\,V^{3+} + 2\,OH^{-}$$

The electrochemical rebalancing method can remove the accumulated hydroxide, repelling $O_2$:

$$2\,OH^{-} \rightarrow \frac{1}{2}O_2 + H_2O + 2\,e^{-}$$

Because the electrolyte of a vanadium redox flow battery is strongly acidic, the hydroxide is readily neutralized and forming water. Hence the oxidation reaction is the following:

$$\frac{1}{2}O_2 + 2V^{2+} + 2H^+ \rightarrow 2V^{3+} + H_2O$$

Therefore, instead of generating two hydroxides in the negolyte, the oxidation by oxygen reaction causes the loss of two protons. And the electrochemical rebalancing method in such scenario is as follows:

$$H_2O \rightarrow \frac{1}{2}O_2 + 2H^+ + 2e^-$$

During the electrochemical rebalancing process, the electrons are transferred to the posolyte side, which has accumulated the oxidized form $VO^{2+}$, through

$$2VO^{2+} + 2e^- \rightarrow 2VO_2^+$$

, and eventually both negolyte and posolyte sides are fully discharged ($VO_2^+$ in posolyte and $V^{3+}$ in negolyte), thus rebalancing the system.

*Inorganic Non-PCET system in basic aqueous solution: air (posolyte) | $S_4^{2-}/S_4^{4-}$ (negolyte) Battery*

When a sulfur-air flow battery[10] is charged: if oxygen diffuses into polysulfide negolyte, oxygen can chemically oxidize polysulfide, and hydroxide is accumulated in the negolyte,

$$\frac{1}{2}O_2 + 2S_4^{4-} + H_2O \rightarrow 2S_4^{2-} + 2OH^-$$

The electrochemical rebalancing method can remove the accumulated hydroxide, repelling $O_2$:

$$2OH^- \rightarrow \frac{1}{2}O_2 + H_2O + 2e^-$$

During the electrochemical rebalancing process, the electrons are transferred to the posolyte side externally, thus rebalancing the system.

*Solid polyquinone Non-PCET system for carbon capture*: *$LiFePO_4$ (cathode) | Polyquinone (anode)*

Liu et al.[11] demonstrated a solid quinone aqueous carbon capture system, where the cathode is $LiFePO_4$ and the anode is polyquinone (PAQ) tethered to a carbon electrode. The authors utilized a 20 molal LiTFSI aqueous solution to ensure that the reduced PAQ are deprotonated, i.e. $PAQ^{2-}$, which then binds with $CO_2$ to form PAQ-$CO_2$ adduct. Although the influence of oxygen in this system is rather small, but side reaction still happens and can cause long term imbalance (accumulation of oxidized cathode material and accumulated LiOH in the anode side).

When the anode is charged: oxygen can chemically oxidize the air-sensitive anode, and hydroxide is accumulated in the negolyte,

$$\frac{1}{2}O_2 + H_2O + PAQ^{2-} \rightarrow PAQ + 2OH^-$$

The electrochemical rebalancing method can remove the accumulated hydroxide, repelling $O_2$:

$$2OH^- \rightarrow \frac{1}{2}O_2 + H_2O + 2e^-$$

During the electrochemical rebalancing process, the electrons are transferred to the cathode side externally, eventually both anode and cathode are discharged, rebalancing the system.

## 4 **Synthesis**

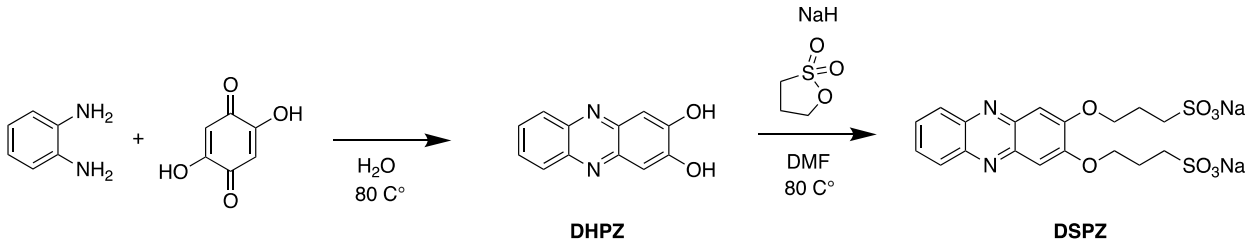


**Schematic S 1| Synthesis of DSPZ.**

Benzene-1,2-diamine (1 equiv.) was mixed with 2,5-dihydroxycyclohexa-2,5-diene-1,4-dione (1.03 equiv.) in water to achieve 0.2 M benzene-1,2-diamine solution in a pressure vessel. The reaction mixture was refluxed at 80 °C and stirred overnight. The resulting slurry was filtered, and the black precipitate was crude product phenazine-2,3-diol (DHPZ). The black precipitate was then dissolved in 0.1 M KOH solution to make a 0.02 M DHPZ solution. The solution was filtered again and the filtrate was acidified with HCl solution until pH reached 7. Red precipitates formed and were filtered to give pure DHPZ (81% yield).

DHPZ (1 equiv. ) was dissolved in DMF to make 0.05 M DHPZ solution. NaH (60 wt. % in mineral oil) (2.2 equiv. NaH) was added to the DHPZ solution under $N_2$. After all bubbles disappeared, 2.05 equiv. propane sultone was then added into the solution. The reaction mixture was stirred overnight at 80 °C to give a red slurry. The slurry was then cooled and filtered. The red precipitates were washed thoroughly with ethyl acetate to remove residual DMF. The final DSPZ products were red solids (65% yield)

## References


1. Roy, R. N.; Roy, L. N.; Vogel, K. M.; Portermoore, C.; Pearson, T.; Good, C. E.; Millero, F. J.; Campbell, D. M., The Dissociation Constants of Carbonic Acid in Seawater at Salinities 5 to 45 and Temperatures 0 to 45 °C. *Mar Chem* **1993,** *44* (2-4), 249-267.
2. Jin, S.; Wu, M.; Gordon, R. G.; Aziz, M. J.; Kwabi, D. G., pH swing cycle for $CO_2$ capture electrochemically driven through proton-coupled electron transfer. *Energy & Environmental Science* **2020,** *13* (10), 3706-3722.
3. Hollas, A.; Wei, X. L.; Murugesan, V.; Nie, Z. M.; Li, B.; Reed, D.; Liu, J.; Sprenkle, V.; Wang, W., A biomimetic high-capacity phenazine-based anolyte for aqueous organic redox flow batteries. *Nat Energy* **2018,** *3* (6), 508-514.
4. Jin, S.; Jing, Y.; Kwabi, D. G.; Ji, Y.; Tong, L.; De Porcellinis, D.; Goulet, M. A.; Pollack, D. A.; Gordon, R. G.; Aziz, M. J., A water-miscible quinone flow battery with high volumetric capacity and energy density. *ACS Energy Letters* **2019,** *4* (6), 1342-1348.
5. Ji, Y.; Goulet, M. A.; Pollack, D. A.; Kwabi, D. G.; Jin, S.; Porcellinis, D.; Kerr, E. F.; Gordon, R. G.; Aziz, M. J., A phosphonate-functionalized quinone redox flow battery at near-neutral pH with record capacity retention rate. *Advanced Energy Materials* **2019,** *9* (12), 1900039.
6. Beh, E. S.; De Porcellinis, D.; Gracia, R. L.; Xia, K. T.; Gordon, R. G.; Aziz, M. J., A Neutral pH Aqueous Organic-Organometallic Redox Flow Battery with Extremely High Capacity Retention. *ACS Energy Letters* **2017,** *2* (3), 639-644.
7. Jin, S.; Fell, E. M.; Vina-Lopez, L.; Jing, Y.; Michalak, P. W.; Gordon, R. G.; Aziz, M. J., Near Neutral pH Redox Flow Battery with Low Permeability and Long-Lifetime Phosphonated Viologen Active Species. *Advanced Energy Materials* **2020,** *10* (20), 2000100.
8. Luo, J.; Hu, B.; Debruler, C.; Bi, Y. J.; Zhao, Y.; Yuan, B.; Hu, M. W.; Wu, W. D.; Liu, T. L., Unprecedented Capacity and Stability of Ammonium Ferrocyanide Catholyte in pH Neutral Aqueous Redox Flow Batteries. *Joule* **2019,** *3* (1), 149-163.
9. Mena, E.; Lopez-Vizcaino, R.; Millan, M.; Canizares, P.; Lobato, J.; Rodrigo, M. A., Vanadium redox flow batteries for the storage of electricity produced in wind turbines. *International Journal of Energy Research* **2018,** *42* (2), 720-730.
10. Li, Z.; Pan, M. S.; Su, L.; Tsai, P. C.; Badel, A. F.; Valle, J. M.; Eiler, S. L.; Xiang, K.; Brushett, F. R.; Chiang, Y. M., Air-Breathing Aqueous Sulfur Flow Battery for Ultralow-Cost Long-Duration Electrical Storage. *Joule* **2017,** *1* (2), 306-327.
11. Liu, Y.; Ye, H.-Z.; Diederichsen, K. M.; Voorhis, T. V.; Hatton, T. A., Electrochemically mediated carbon dioxide separation with quinone chemistry in salt-concentrated aqueous media. *Nature Communications* **2020,** *11*, 2278.